HHS Public Access

Author manuscript

Cell Metab. Author manuscript; available in PMC 2021 November 03.

Published in final edited form as:

Cell Metab. 2020 November 03; 32(5): 801–813.e6. doi:10.1016/j.cmet.2020.09.011.

Ablation of Fat Cells in Adult Mice Induces Massive Bone Gain

Wei Zou[1,2], **Nidhi Rohatgi**[1], **Jonathan R. Brestoff**[3], **Yongjia Li**[1], **Ruteja A Barve**[4], **Eric Tycksen**[4], **Yung Kim**[5], **Matthew J. Silva**[2,5,6], **Steven L. Teitelbaum**[1,2,7]

[1]Division of Anatomic and Molecular Pathology, Department of Pathology and Immunology, Washington University School of Medicine, St. Louis, MO 63110, USA

[2]Musculoskeletal Research Center, Washington University School of Medicine, St. Louis, MO 63110, USA

[3]Division of Laboratory and Genomic Medicine, Department of Pathology and Immunology, Washington University School of Medicine, St. Louis, MO 63110, USA

[4]Department of Genetics, Washington University School of Medicine, St. Louis, MO 63110, USA

[5]Department of Orthopaedic Surgery, Washington University School of Medicine, St. Louis, MO 63110, USA

[6]Department of Biomedical Engineering, Washington University School of Medicine, St. Louis, MO 63110, USA

[7]Division of Bone and Mineral Diseases, Department of Medicine, Washington University School of Medicine, St. Louis, MO 63110, USA

Summary

Adipocytes control bone mass but the mechanism is unclear. To explore the effect of post-natal adipocyte elimination on bone cells, we mated mice expressing an inducible primate diphtheria toxin receptor (DTR) to those bearing adiponectin (ADQ)-Cre. DTR activation eliminates peripheral and marrow adipocytes in these DTR^{ADQ} mice. Within 4 days of DTR activation, the systemic bone mass of DTR^{ADQ} mice began to increase due to stimulated osteogenesis, with a 1000% expansion by 10–14 days post-DTR treatment. This adipocyte ablation-mediated enhancement of skeletal mass reflected bone morphogenetic protein (BMP) receptor activation following elimination of its inhibitors, associated with simultaneous EGF receptor signaling.

Corresponding author: Steven L. Teitelbaum, Washington University School of Medicine, Department of Pathology and Immunology, Campus Box 8118, 660 South Euclid Avenue, St. Louis, MO 63110, Phone: (314) 454-8463, Fax: (314) 454-5505, teitelbs@wustl.edu.

Author Contributions

W.Z. designed and performed experiments and analyzed all data and wrote the manuscript. N.R., J.R.B, Y.L., Y.K. performed experiments, R.A.B and E.T analyzed the RNAseq data, M.J.S. designed experiments and wrote the manuscript. S.L.T. designed experiments and wrote the manuscript.

Declaration of Interests

R.A.B. may receive royalty income based on the CompBio technology developed by R.A.B. and licensed by Washington University to PercayAI. All other authors declare no competing interests.

DTR^{ADQ}-induced osteosclerosis is not due to ablation of peripheral adipocytes but likely reflects elimination of marrow ADQ-expressing cells. Thus, anabolic drugs targeting BMP receptor inhibitors with short term EGF receptor activation may be a means of profoundly increasing skeletal mass to prevent or reverse pathological bone loss.

Graphical Abstract

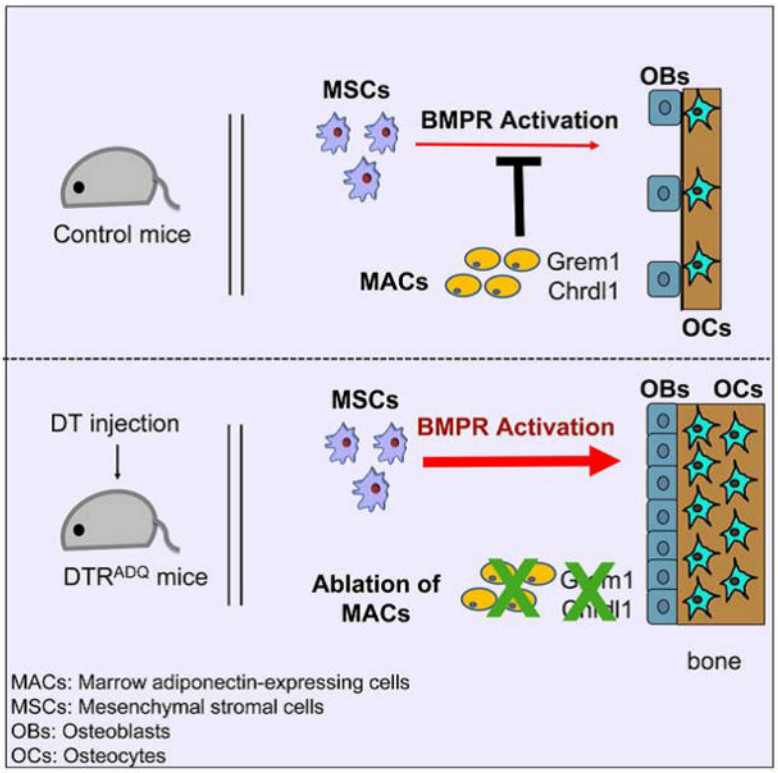

Introduction

The influence of adipose tissue on the skeleton is apparent as obesity generally predisposes to increased bone mass. While this has been assumed to reflect the biomechanical influence of weight, there is now evidence of a metabolic relationship between fat tissue and the skeleton in which bone cells influence adipocyte function and adipocyte-derived cytokines (so-called ‘adipokines’), as well as the release of lipid stores, regulate osteoblasts and osteoclasts (Ducy et al., 2000; Elefteriou et al., 2004; Ferron et al., 2010; Kajimura et al., 2013; Rendina-Ruedy and Rosen, 2020). Thus, understanding the mechanisms by which the products of adipocytes control bone cells may lead to new anti-osteoporosis therapeutic strategies. In fact, we previously demonstrated that germline deletion of white and brown adipose tissue (WAT and BAT, respectively), by expressing diphtheria toxin (DT) exclusively in fat, substantially enhances bone mass (Zou et al., 2019). The increased skeletal mass of these “fat free” mice suggests that targeting the products of adipose tissue may be exploited therapeutically to prevent or restore bone loss. The medicinal significance of the fat free mouse is limited, however, by its germline induction of fat depletion, which occurs during

embryogenesis. To obviate this limitation and produce a model more therapeutically relevant, we generated mice in which fat ablation is induced in adults. To this end, we mated mice expressing the primate diphtheria toxin receptor (DTR), under control of a Stop-flox cassette to those expressing adiponectin (ADQ)-Cre. As such, DT administration completely eliminates the WAT and BAT in these DTR^{ADQ} mice and ablates marrow adipocytes.

In keeping with our hypothesis that modified abundance of adipocyte-derived products, altered upon cell death, positively impacts the skeleton, we found in this study that the mass of the medullary bone of DTR^{ADQ} mice increased 10-fold within 10 days of DT, significantly enhancing its mechanical properties. In fact, the increase in systemic bone mass, induced by DTR-induced adipocyte ablation, is the most rapid and robust observed in any model reported to date and prevents ovariectomy-induced and age related osteoporosis.

Our findings show that bone marrow adipose tissue regulates skeletal mass and that this regulation can be beneficially disinhibited to promote the growth of stronger bones. Gaining a deeper understanding of the molecular mechanism for this phenomenon will perhaps allow for its pharmacological replication and achievement of a durable and potent pro-anabolic therapy for pathological bone loss.

Results

Ablation of fat in adult mice leads to osteosclerosis

Given the increase in bone mass attending germline deletion of fat, we hypothesized that post-natal adipose tissue ablation would do the same. To test this hypothesis we mated mice bearing primate DTR, downstream of a floxed stop codon (DTR-$STOP^{fl/fl}$), to those expressing adiponectin-Cre (ADQ-Cre) (DTR^{ADQ} mice) (Lee et al., 2013). Administration of DT is non-toxic in naive mice and exclusively targets cells over-expressing transgenic primate DTR. Thus, DT given to 2 month old DTR^{ADQ} mice (DT/ DTR^{ADQ} mice) virtually eliminates WAT BAT leading to an absence of detectable serum adiponectin (Fig S1A,B, Table S1) and increased serum Lactate Dehydrogenase (LDH) level, which likely represents the virtually complete ablation of peripheral fat depots (Fig S1C). After 10 days of DT administration we performed radiographic and microCT (μCT) analyses and found that bone occupied essentially the entire endocortical space from the metaphysis through the diaphysis (Fig 1A–C, S1D). An abundance of new bone matrix was histologically apparent within 3–4 days of DT administration, at which time marrow adipocytes were no longer evident nor was there evidence of marrow necrosis (Fig 1D, S1E). We next confirmed ablation of marrow adipocytes by osmium tetroxide staining followed by μCT imaging (Scheller et al., 2014) (Fig 1E).

The abundant bone matrix apparent after 4 days of DT treatment was likely not yet mineralized as it was not evident by μCT examination until day 7 (Fig 1B). At 10 days, we confirmed by histology, x-ray and uCT that virtually the entire endocortical space was occupied by trabecular bone (Fig 1D). Cortical bone was also markedly increased due to endocortical ossification. Due to their merging, compact and newly formed trabecular bone could not be accurately distinguished by μCT. This profound osteosclerosis was also present in vertebrae (Fig 1F). DT/DTR^{ADQ} prevented ovariectomy induced osteoporosis (Fig 1G,

S1F) and markedly increased bone mass of 1 year-old mice but less so than that of those in 2 month-old mice (Fig 1H, S1G).

We next confirmed by μCT analysis of the femoral diaphysis, that the augmented endosteal bone in DT/DTR^{ADQ} mice, was evident as increased bone area, reduced medullary area and normal total area (Fig. 2A–C). We performed femoral bending tests which revealed bones of DTR^{ADQ} mice, following 10 days of DT administration, had increased stiffness, yield force, maximum force, ranging 40–70% higher than control, indicating enhanced mechanical function (Fig. 2D–F). Notably, the post-yield displacement, a measure related to bone quality, was unaffected (Fig. 2G). Thus, the medullary osteosclerosis of the DT/DTR^{ADQ} mice resulted in markedly enhanced whole-bone mechanical properties, confirming the new bone is structurally integrated and provides mechanical benefit.

DT/DTR^{ADQ} osteosclerosis is due to enhanced osteoblast recruitment and differentiation

We next assayed serum P1NP levels, a marker of osteogenesis and found that it was increased 7 days after DT administration (Fig 3A). Marrow alkaline phosphatase mRNA, a marker of osteoblast activity was also enhanced (Fig 3B). DT/DTR^{ADQ} induction of profound osteogenesis occurred rapidly and was attenuated within 2 weeks. This pattern of P1NP normalization was similar to that occurring in patients with osteoporosis treated with the anti-sclerostin monoclonal antibody, romosozumab, in which the bone formation normalizes after 3–6 months of therapy (McClung et al., 2018).

To further determine the contribution of increased bone formation to adipocyte ablation-stimulated osteosclerosis, we mated DTR^{ADQ} to 2.3Col–GFP reporter mice to genetically mark mature osteoblasts (Roeder et al., 2016). Four days after DT-induced adipocyte ablation, many GFP+ cells appeared in DTR^{ADQ} mice (Fig 3C). Suggesting adipocyte ablation also promoted immature (i.e. mitotic) progenitors, CFU-OBs generated from crushed periosteum-stripped femur progressively increased with time of DT administration (Fig 3D). Immunostaining DT/DTR^{ADQ}/2.3Col–GFP bone for the proliferation marker, PCNA, revealed only a minimal number of GFP+ cells were replicating (Fig 3E). There was, however, an abundance of GFP−negative, PCNA+ (i.e. dividing) cells juxtaposed to GFP+ mature osteoblasts. These data suggest that in addition to accelerating differentiation of post-mitotic osteoblast progenitors, DT/DTR^{ADQ} adipocyte ablation increased immature pre-osteoblast abundance. To verify this is so we mated DTR^{ADQ} 2.3Col-GFP mice to those expressing thymidine kinase (TK) under control of the 3.6Col1a1 promoter (TK-3.6Col1a1 mice), which is specifically transduced by mitotic pre-osteoblastic cells (Jilka et al., 2009). Immunostaining revealed an abundance of TK-positive cells juxtaposed to those expressing 2.3Col-GFP (Fig 3F). Confirming the necessity of early pre-osteoblasts, DT/DTR^{ADQ}-induced osteosclerosis was eliminated in TK-3.6Col1a1 mice by ganciclovir which targeted only replicating pre-osteoblastic cells in these mice (Fig 3G–I, S2). In sum, these data indicate DT/DTR^{ADQ}-mediated fat ablation promoted an abundance of mitotic pre-osteoblastic cells and their rapid differentiation into mature osteoblasts.

After 10–14 days of DT administration, at which time peak bone mass was achieved, it declined but stabilized at approximately 300–400% above control for at least 3 months (Fig 4A, S3A). The loss of bone was associated with marked osteoclastogenesis (Fig 4B, S3B)

and resorptive activity (Fig 4C). While receptor activator of NF-κB ligand (RANKL) expression did not change with DT treatment (Fig S3C), osteoprotegerin (Opg) diminished, indicating enhanced osteoclast formation and bone resorption were due to decreased abundance of the RANKL decoy receptor (Fig 4D). The fall in peak bone mass likely reflecting accelerated resorption raised the possibility the process can be prevented by arresting osteoclastogenesis. Thus, we administered OPG-Fc or carrier to DTR^{ADQ} mice for 20 days beginning at day 10 of DT injection. While maximally achieved bone mass declined approximately 50% after one month of DT administration in PBS injected mice, it actually increased 1/3 in those receiving OPG-Fc (Fig 4E, F, S3D). To determine if recovery of adipose tissue may contribute to the reduction of peak bone mass, we measured body fat pads (BAT, iWAT and eWAT) and marrow adipocytes of DTR^{ADQ} mice after 2 months of daily DT injection. While BAT and WAT weight remained statistically less than PBS-injected control, there was a tendency to increase after 2 months. Marrow adipocytes, however, remained essentially absent (Fig S3E, Table S1). Thus, the ultimate decline in peak bone mass in DT/DTR^{ADQ} mice reflected stimulated osteoclastogenesis, which can be therapeutically prevented. Surprisingly, despite the decline in peak trabecular bone mass at 10–14 days, cortical thickness was significantly greater and associated with profoundly enhanced bone strength, after 2 months of DT injection (Fig 4G, H). This observation is consistent with a return to normal remodeling initiated by osteoclasts, thus enhancing bone quality.

DT/DTR^{ADQ} osteogenesis is not mediated by loss of peripheral adipose tissue

In keeping with their lipodystrophic state, DT/DTR^{ADQ} mice developed the metabolic syndrome as manifested by hyperglycemia and hepatic steatosis, raising the possibility that the products of insulin-resistant diabetes, which may enhance bone mass, contributed to the osteosclerotic phenotype. Proving that attendant type 2 diabetes did not mediate adipocyte ablation-enhanced bone formation, WT WAT, transplanted into DT/DTR^{ADQ} mice, normalized their serum glucose and eliminated hepatic steatosis but did not affect their osteosclerosis (Fig 5A,B, S3F). Failure of transplanted WAT to prevent DT/DTR^{ADQ}-mediated osteosclerosis also suggested the osteogenic process was not induced by absence of the products of peripheral fat depots and called into question the significance of the trended increase in BAT and WAT after 2 months. This conclusion was supported by failure of DT-activated DTR^{ADQ} adipose tissue, transplanted into WT mice to alter bone mass (Fig 5C). To further explore this issue, we parabiosed WT and DTR^{ADQ} mice. Consistent with a common vasculature, administration of DT to control mice promoted DTR^{ADQ} osteosclerosis. Indicating that the osteogenic inducing product(s) did not circulate and thus was likely not derived from peripheral fat, DT injected into the parabiosed DTR^{ADQ} mouse, induced osteosclerosis but did not impact bone mass of its WT partner (Fig 5D). Thus, DT/DTR^{ADQ} osteogenesis did not appear to be mediated by peripheral adipose tissue.

BMPR signaling mediates adipocyte ablation-induced osteosclerosis

To gain insight into the signaling events by which DT/DTR^{ADQ}-mediated adipocyte ablation promotes osteogenesis we performed RNAseq of marrow prior to and after 1–3 days of DT injection. This exercise confirmed ablation of marrow adipocytes, as adiponectin expression was markedly reduced while enhanced expression of Col1a1 and Col1a2 genes was in

keeping with stimulated osteogenesis (Fig 6A, S4A). RNAseq CompBio analysis also indicated that DT/DTR^{ADQ}-induced osteogenesis was likely mediated by BMPR signaling enhanced by downregulating BMP inhibitors (Fig 6B, Table S2). For example, there was suppressed genetic expression of the specific BMPR inhibitors, chordin-like1 (CHRDL1) and gremlin1 (GREM1). Importantly, GREM1 deficiency contributes to the massive osteogenesis of the BMP-induced disease fibrodysplasia ossificans progressive (FOP) (Ahn et al., 2003), and its overexpression promotes bone loss and fracture (Gazzerro et al., 2005). Alternatively, there was increased expression of the BMPR activator, WISP1/CCN4 (Ono et al., 2011). These RNAseq changes in adiponectin, GREM1, CHRDL1 and Wisp1 expression were confirmed by qPCR (Fig 6C). qPCR of marrow also documented no increase in TNFα, IL-1β or IL-6 (Fig 6D), which taken with the absence of histological necrosis, indicated the robust osteogenesis did not reflect inflammation. Further indicating that GREM1 and CHRDL1 deficiency in marrow of DT/DTR^{ADQ} mice was due to marrow adipocyte ablation, both BMPR inhibitors were robustly expressed by MSCs induced to express adiponectin *in vitro*, but not their naive precursors (Fig 6E). Phosphorylation of Smads 1, 5, and 8, the canonical targets of BMPR-1 activation, were progressively increased in DTR^{ADQ} marrow within the first 3 days of DT administration (Fig 6F). Immunostaining of phosphorylated Smad1, 5 and 8 confirmed their abundance in DT/DTR^{ADQ} marrow and the proximity of the cells to the bone surface and mature (2.3Col-GFP+) osteoblasts (Fig 6G). Smad1,5,8 immunostaining was not evident within 2.3Col-GFP+ cells, indicating BMPR activation affected earlier osteoblast precursors, likely promoting their differentiation. Establishing BMPR signaling was essential, 10 days administration of LDN-193189 (3 mg kg^{-1} i.p. q 12 hrs.), a selective BMPR inhibitor with the potential to treat FOP (Williams and Bullock, 2018), prevented DT/DTR^{ADQ} adipocyte ablation-induced osteosclerosis (Fig 6H,I, S4B).

We next explored if post-natal depletion of fat by means other than DT/DTR^{ADQ} enhanced bone mass. To this end, we mated mice expressing DT, under control of a STOP-flox cassette, to those bearing tamoxifen (TAM)-inducible ADQ-CreER (DT^{ADQER}). DT^{ADQER} mice were administered TAM to stimulate DT expression in adipocytes (TAM/DT^{ADQER}). As evidenced by a virtual absence of serum adiponectin and significant decrease of fat pad weight, peripheral fat was targeted in TAM/DT^{ADQER} animals (Fig S5A, S5B, Table S1). In contrast to DT/DTR^{ADQ} mice, TAM/DTA^{ADQER} fat-depleted mice exhibited no alteration of bone mass (Fig S5C, S5D). Also unlike DT/DTR^{ADQ} mice, in which marrow adipocyte ablation was complete, these cells in TAM/DTA^{ADQER} mice were not deleted as effectively although there was a non-statistically significant trend towards diminution (Fig S5E). Importantly, marrow adiponectin gene expression was unaltered as was that of GREM1 and CHRDL1 (Fig S5F). Thus, the osteogenic failure of depletion of peripheral fat, while preserving marrow adipocytes, was consistent with ablation of the latter being responsible for activating BMPR signaling.

In contrast to arrest of BMPR, administration of the tankyrase1/2 inhibitor, XAV-939, by a strategy established to arrest osteogenesis in other circumstances, had no effect on that induced by DT/DTR^{ADQ} (Fig S6), suggesting Wnt, the most common osteogenic pathway, may not be involved (Xu et al., 2017). In sum, these data indicate BMPR was an essential component of adipocyte ablation-induced osteogenesis.

EGF receptor signaling partners with BMPR signaling to promote adipocyte ablation-induced osteogenesis

The fact that DTR and its cleaved (i.e. mature) product, function as growth factors (Ding and Morrison, 2013; Higashiyama et al., 1995; Miyoshi et al., 1997; Nakamura et al., 1995; Takemura et al., 1997) raised the prospect that upon, release from adipocytes undergoing ablation, it activated EGFR which contributed to the osteogenesis of DT/DTR^{ADQ} mice. Supporting the hypothesis that the growth factor properties of adipocyte ablation-mobilized DTR activated EGFR signaling we found the pharmacological EGFR inhibitor, gefitinib, markedly arrests DT/DTR^{ADQ}-induced osteogenesis (Fig 7B,C, S7A). Indicating that DTR (i.e., HB-EGF) requires adipocyte ablation, and thus suppressed expression of BMPR inhibitors GREM1 and CHRDL1, to promote osteogenesis, DT-induced death of B cells expressing DTR, mediated by CD19-Cre, did not impact the skeleton nor did it diminish GREM1 and CHRDL1 or increase Wisp1 marrow expresssion (Fig 7D–F, S7B).

Discussion

Osteoporosis is endemic in western and Asian societies and its predisposition to fracture is a major mortality risk to older individuals. The appreciation, in recent years, of metabolic cross talk between bone and adipose tissue has prompted exploration of the responsible mechanisms with the aim of therapeutically exploiting this information.

Regardless of cause, osteoporosis represents enhanced osteoclast activity relative to that of osteoblasts. Thus, therapeutic strategies involve either anti-resorptive or pro-osteogenic (i.e., anabolic) drugs, often administered sequentially. Likely due to suppressed remodeling, the quality of bone induced by anti-resorptive agents is often compromised and may predispose to atypical fractures (McClung, 2013). Because this does not occur in the context of pharmacological bone anabolism, agents which stimulate osteoblasts are in demand. In fact, the development of romozosumab, an FDA approved humanized anti-sclerostin antibody, is a paradigm for our efforts as it reflects delineating the mechanism of the pathologically accelerated bone formation of sclerosteosis, in which a fracture has never been reported (Appelman-Dijkstra and Papapoulos, 2016; van Lierop et al., 2017), and extending it therapeutically. Thus, exploiting the means by which this uniquely rapid and profound systemic bone formation occurs may have therapeutic relevance.

To gain insight into the molecular mechanisms driving the profound osteogenesis of our adult model, we performed RNAseq analysis of DTR^{ADQ} marrow within the first 3 days of DT administration. Suppression of GREM1 (Gazzerro et al., 2007; Hu et al., 2017) and CHRDL1 (Troilo et al., 2015; Wang et al., 2018) as well as enhanced expression of Wisp-1, indicates that activation of their targeted BMPR signaling pathway is likely involved in the profound osteogenesis. Our findings that both GREM1 and CHRDL1 are products of adiponectin-expressing cells raises the possibility that absence of fat in DT/DTR^{ADQ} mice prevents induction of these BMPR inhibitors resulting in arrest of negative feedback (Pereira et al., 2000). The participation of BMPR activation, in DT/DTR^{ADQ} -induced osteogenesis, is fortified by phosphorylation of Smads 1,5 and 8 which represent canonical markers of the pathway's activation. Unexpectedly, Smad1,5,8 staining is not visible in cells expressing 2.3Col–GFP, suggesting BMPR activity is more robust in immature cells which are

stimulated to undergo differentiation into mature osteoblasts. Most importantly, LDN-193189, a selective BMPR1 inhibitor used to treat FOP, virtually arrests DTRADQ-mediated osteogenesis. Thus, BMPR signaling is activated in DT/DTR^{ADQ} mice and its pharmacological inhibition prevents the osteosclerotic phenotype.

Wnt signaling is the most commonly activated osteogenic pathway. Unexpectedly, despite the broad effect of Wnts on bone formation and the induced expression of its product, Wisp-1, a tankyrase1/2 inhibitor, which targets Wnt activation, does not impact DT/DTR osteogenesis. This observation underscores the abundance of data establishing the context dependency of BMPR/Wnt interaction, which in some circumstances is inhibitory and in others, stimulatory (Lin and Hankenson, 2011; Marcellini et al., 2012; Voorneveld et al., 2015).

While therapeutic attention of BMPR signaling has largely focused on its systemic inhibition in circumstances such as FOP or focal stimulation in fracture repair and bone grafting (Lowery and Rosen, 2018), our studies fortify the possibility that BMPR activation, in specific context, may increase systemic bone mass in osteoporosis. The consequences of BMPR activation are complex as the magnitude of osteogenesis varies with selective inductive ligands, particularly post-natally (Lowery and Rosen, 2018). Much of the confusion regarding systemic anabolic effects of BMPR activation, in adults, is likely due to the fact that the majority of related studies involve loss-of-function rather than gain-of-function models. Interestingly, those mutants which induce profound BMPR-mediated osteogenesis, yield an abundance of extraskeletal endochondral bone formation, which in the case of FOP, is crippling. In contrast, the profound osteogenesis of DT/DTR^{ADQ} mice, which substantially enhances skeletal strength, appears to be entirely membranous with no μCT evidence of extraskeletal deposition, an observation of potential clinical relevance. Additionally, DT/DTR^{ADQ} marrow exhibits no morphological evidence of necrosis nor are inflammatory cytokines increased. Taken with the fact that it suppresses rather than enhances bone formation, inflammation does not contribute to the induced osteogenesis (Hardy and Cooper, 2009).

Our data indicate that both EGFR and BMPR may participate in DT/DTR^{ADQ}-induced osteogenesis. Collaboration between these two signaling pathways is effective in bone repair but no information exists regarding their combined systemic impact (Lee et al., 2015). In fact, EGFR activation targets the skeleton as it induces proliferation of osteogenic precursors, as occurs in DT/DTR^{ADQ} mice (Schneider et al., 2009) and may be essential to the bone anabolic effect of PTH (Zhu et al., 2012). Additionally, EGFR deletion in osteoblasts promotes osteoporosis (Linder et al., 2018). On the other hand, EGFR blunts osteoblast differentiation, indicating that the marked increase in number of these bone forming cells in DT/DTR^{ADQ} mice may reflect dominant BMPR stimulation by depletion of its inhibitors (Laflamme et al., 2010). The stimulatory role of EGFR is supported by induction, in DT/DTR marrow, of Egr2, a principal product of the activated pathway which enhances bone formation (Chandra et al., 2013; Shukla et al., 2017). Most convincing of the importance of EGFR activation in DT/DTR^{ADQ}-induced bone formation, gefitinib, an FDA approved anti-EGFR drug, arrests the osteogenic event. EGFR activation is necessary for

DT/DTR^{ADQ}-induced osteogenesis, but its role may be to deplete GREM1 and CHRDL1 by ablating adipocytes, thereby profoundly activating BMPR signaling.

An essential issue of our observations is the adipocyte source of DT/DTR^{ADQ}-induced osteogenesis. Whereas the osteosclerosis of our germline fat free osteosclerotic mice is reversible by transplantation of WT peripheral WAT, this strategy does not impact the enhanced skeletal mass induced by DTR^{ADQ} activation (Zou et al., 2019). Additionally, parabiosis of WT and DTR^{ADQ} mice yields no evidence of a systemic factor influencing bone mass, which would be expected if the responsible tissue was peripheral fat. These observations suggest ablation of marrow adipocytes is the likely mediator of DTR^{ADQ} osteogenesis. This conclusion is consistent with selective targeting of WAT by TAM/DT^{ADQER} (Sassmann et al., 2010), which ablates peripheral but not all marrow fat, and does not induce osteogenesis. While abundance of marrow adipocytes is associated with changes in bone mass in conditions such as estrogen deficiency and aging, there is currently little evidence of a causal relationship which the current data provide (Rendina-Ruedy and Rosen, 2020). The failure of stimulated TAM/DT^{ADQER} to reduce marrow GREM1 and CHRDL1, as well as our documentation that these BMPR inhibitors are expressed, *in vitro*, by adipocytes generated from marrow-derived precursors, is consistent with marrow fat regulating bone mass via BMPR signaling. While it is unlikely that adipocyte ablation will be utilized to enhance bone mass in patients, similar to development of romozosumab, which was based upon the pathogenesis of sclerosteosis, there is a reasonable possibility that insights into the mechanisms of this most robust form of systemic osteogenesis, will lead to bone anabolic drugs (Appelman-Dijkstra and Papapoulos, 2016). Our present hypothesis holds that such agent(s) will entail relatively short-term EGFR activation combined with suppression of adipose tissue-expressed BMPR inhibitors, particularly CHRDL1 and GREM1. Thus, combined suppression of GREM1 and CHRDL1 may provide a foundation for osteogenic drug development.

The 1000% escalation of bone mass, occurring within 10–14 days of DTR activation, is followed by a rapid decline although it is maintained at approximately 400% above control. The attendant increase in osteoclast number, a reflection of decreased OPG expression, suggests that anti-resorptive therapy may arrest this decline and such proved to be true. More significantly, despite the decline in trabecular bone mass shortly after it peaks, cortical thickness substantially increases. While to be proven, these structural changes may reflect return of normal remodeling and incorporation of induced trabeculae into the cortical endosteum. This hypothesis is consistent with histologically evident melding of trabecular and cortical bone early in DTR activation. The substantial increase in biomechanical strength after 2 months, despite trabecular bone loss, suggests short pharmacological BMPR/EGFR activation may be uniquely potent in reversing osteoporosis.

The EGF family of growth factors, including HB-EGF, are potent inducers of wound healing. In fact, recombinant EGF (Heberprot-P) is used to treat diabetic foot ulcers (Yamakawa and Hayashida, 2019). EGFR activation is, however, associated with neoplasia raising a theoretical limitation to stimulating EGFR/BMPR signaling to treat skeletal disorders. On the other hand, all FDA-approved bone anabolic agents faced this limitation. For example, teriparatide, induces osteosarcoma in rats. While this complication has not

been noted in patients, administration of the drug is limited to 2 years and avoided by those with a predisposition to cancer. Rats administered abaloparatide similarly develop osteosarcoma (Jolette et al., 2017). Perhaps more relevant to our observations is romozosumab, which activates the Wnt pathway via LRP5/6, implicated in the pathogenesis and compromised prognosis of a variety of human cancers including triple negative breast and colon cancer (Ma et al., 2017; Roslan et al., 2019; Schatoff et al., 2017). Additionally, Wnt activation in cancer cells promotes bone metastasis (Esposito et al., 2019). Because of the pathway's established hyperactivation, a variety of Wnt inhibitors are in anticancer clinical trials (Krishnamurthy and Kurzrock, 2018; Takebe et al., 2015). Perhaps because its targeting of bone cells overrides Wnt-induced neoplastic properties, unexpectedly, romozosumab may actually retard skeletal metastasis (Hesse et al., 2019). Thus, like teriparatide, abaloparatide, and romozosumab, whose duration of administration is FDA limited and whose increased bone mass is maintained by anti-resorptive drugs (Black et al., 2005; Cosman et al., 2017; Horne et al., 2018), the same may hold for an EGFR/BMPR-based therapy that is ultimately derived from the mechanistic insights of this study. Even so, the profound rapidity and apparent stability of EGFR/BMPR-induced osteogenesis suggests that a short duration of administration of such derivative drugs to patients, followed by anti-resorptive therapy, may be an efficacious strategy for treating osteoporosis.

Limitations of Study

While the present study confirms that elimination of adiponectin-expressing cells can promote uniquely profound osteogenesis, many issues, such as the mechanistic relationship between BMPR and EGFR stimulation, remain to be addressed. Most importantly, however, while activated DTR^{ADQ}-induced osteosclerosis is BMPR mediated, presumably due to GREM1 and CHRDL1 depletion, direct proof of their role in the process is lacking as are data documenting the effects of blocking the inhibitors, in marrow, in the absence of EGFR stimulation. This deficiency reflects, in part, absence of an *in vitro* model in which the mechanism by which activated DTR^{ADQ}-mediated enhanced bone mass can be further explored. In keeping with these limitations, the cellular source of GREM1 and CHRDL1 is unresolved, especially as marrow cells, other than adipocytes, are targeted by ADQ-Cre (Mukohira et al., 2019). Resolution of this deficiency is important as therapeutic adaptation of our observations is likely to depend on arrest of these inhibitors.

STAR Methods

RESOURCE AVAILABILITY

Lead Contact—Further information and requests for resources and reagents should be directed to and will be fulfilled by the Lead Contact, Steven L. Teitelbaum (teitelbs@wustl.edu).

Materials Availability—Mouse lines generated in this study (DTR^{ADQ}, DTR^{CD19}, DTR^{ADQ}/Col1–2.3 GFP/Col1–3.6 TK, iDTA/Adipoq Cre/ERT2) are available from the lead contact upon request.

Data and Code Availability—The raw data for the RNA sequencing data reported in this paper have been deposited to the NCBI's Gene Expression Omnibus (GEO) repository, the accession number is GEO: GSE154800.

EXPERIMENTAL MODEL AND SUBJECT DETAILS

Experimental Models and Subject Details—The following mice: iDTR (Lox-Stop-Lox-ROSA-DTR, Cat. 007900), Col1a1*2.3GFP reporter (cat. 013134), CD19 Cre (Cat. 006785), Adipoq Cre (Cat. 010803), Adipoq Cre/ERT2 (cat. 025124) and Rosa-DTA (Lox-Stop-Lox-ROSA-DTA, Cat 010527) were purchase from JAX; TK-3.6Col1a1 mice (Jilka et al., 2009) were kindly provided by Robert Jilka and Charles O'Brien (University of Arkansas). All animals were housed in the animal care unit of Washington University School of Medicine, where they were maintained at 22° C in a 12-hour light-dark cycle according to guidelines of the Association for Assessment and Accreditation of Laboratory Animal Care.

All mice used for experiment were health and had free access to water and food. All mice were from in house matings. Although no gender differences exist in phenotype, male mice were exclusively used except in OVX and parabiosis experiments wherein female mice are required. Animal work was performed according to the policies of Animal Studies Committee (ASC) at Washington University School of Medicine in St. Louis. Mice were analyzed under approved protocols and were provided appropriate care while undergoing research which complies with the standards in the Guide for the Use and Care of Laboratory Animals and the Animal Welfare Act.

DTR^{ADQ} mice were generated by mating homozygous iDTR mice to those expressing adipoq-Cre. DTR^{CD19} mice were generated by mating homozygous iDTR mice to CD19-Cre. Quadruple heterozygous mutant (DTR^{ADQ}/Col1–2.3 GFP/Col1–3.6 TK) mice were bred by cross-mating iDTR/adipoq Cre/Col1–2.3 GFP+ male with transgenic Col1–3.6 TK females in view of previous evidence for tk transgene-induced sterility in males (Al-Shawi et al., 1988).To induce Cre positive cell deletion, Diphtheria toxin (Biological List laboratories) (100ng/mouse/day) was daily i.p. injected into mice. Cre negative littermate got same amount of DT as control.

Tamoxifen inducible fat deletion mice were generated by mating homozygous Lox-stop-Lox-ROSA-DTA mice to Adipoq Cre/ERT2 and Tamoxifen (20mg/ml in coin oil, 100 μl/mouse/day) were i.p. injected into mouse for 5 consecutive days. CreER negative littermate got same amount of Tamoxifen as control.

Ganciclovir was given at 8 μg/g i.p. twice daily in saline; Gefitinib was given at 100mg/Kg i.p. daily; LDN193189 was given at 3mg/Kg i.p. twice daily and XAV-939 was given at 10mg/Kg i.p. daily. Chemicals were injected into mice 1 day prior DT injection. OPG-Fc was given at 100 μg/mouse i.v. twice weekly.

Cell culture—Cells were grown at 37°C in a 5% CO_2 humid atmosphere. ST2 cells (ATCC, CVCL-2205) were cultured in DMEM with 10% FBS, 100 u/ml penicillin and 100μg/ml streptomycin.

Method Details

RNA Extraction and quantitative qPCR—Total RNA from fresh bone marrow or bone was extracted using Trizol following RNA purification with RNeasy RNA purification kit and RNase free DNase digestion (Qiagen). Complementary DNA (cDNA) was synthesized from 1 μg of total RNA using the iScript cDNA synthesis kit (Bio-Rad). Quantitative qPCR was performed using the PowerUp SYBR Green Master Mix kit (Applied Biosystems) according to the kit instruction and gene specific primers. All genes amplicon length is less than 150 nucleotides. PCR reactions for each sample were performed with 7500 fast Real-Time PCR System (Applied Biosystems, Foster City, CA, USA) using the comparative threshold cycle (Ct) method for relative quantification. The glyceraldehyde-3-phosphate dehydrogenase (*Gapdh*) gene was used as an endogenous control.

Flow cytometry—Single cell suspensions of immune cells were prepared from spleens and bone marrow (femur) as previously described (Li et al., 2019; Rohatgi et al., 2018). Cells were treated with Fc Block and then stained with rat anti-mouse CD45-APC (1:200, clone 30-F11; BioLegend), rat anti-mouse CD19-APC/Fire750 (1:300, clone 6D5; BioLegend), and rat anti-mouse B220-PE (1:300, clone RA3–6B2; BioLegend) as previously described (Li et al., 2019; Rohatgi et al., 2018). Events were acquired on a BD X20 flow cytometer, using CountBright Absolute Counting Beads (ThermoFisher) according to the manufacturer's protocol, except that 25 μL was used per sample. B cells were defined as CD45+ CD19+ B220+ cells.

Serum assay—Blood was collected retro-orbitally under anesthesia. Serum was obtained using serum separator tubes (Becton Dickinson) and kept at −80C. P1NP ELISA kit and CTX-1 RatLaps kit were purchased from ids (Immunodiagnosticsystems). LDH assay kit was purchased from BioVision Incorporated.

GTT—Glucose tolerance tests (GTT) were performed in clean cages subjected to starvation with free access to water for 6 hours. Mice were weighed and a small amount of blood was obtained from tail vein for baseline (time 0) glucose measurement. Mice were then injected intraperitoneally with 50% sterile dextrose (1 mg/g body weight). Tail blood glucose was determined at 15, 30, 60, 90 and 120 min after challenge using a Bayer Contour glucometer.

Microcomputed tomography (μCT)—Trabecular bone was scanned using μCT40 scanner (Scanco Medical AG, Bassersdorf, Switzerland; 70 kVp, 114 μA, 300 ms integration time, 16 μm voxel size). A lower threshold of 180 was used for evaluation of all scans. Whole femur through metaphasis and diaphysis were analyzed for trabecular, starting with the first slice in which condyles and primary spongiosa were no longer visible. 50 slices were analyzed for midshaft cortical bone.

Radiographs—Radiographs were taken using Faxitron UltraFocus^{DXA} (Faxitron) according to the manufacturer's instructions.

Marrow Fat osmium staining and μCT—marrow fat osmium was stained with osmium tetroxide according to previously described (Scheller et al., 2015). Briefly, bones were fixed

in 10% neutral-buffered formalin for 24 hours and decalcified in 14% EDTA, pH 7.4, for 3 weeks. Then bones were stained in 1% osmium tetroxide (Electron Microscopy Services, Hatfield, PA; cat.no. 19170) at Sorensen's phosphate buffer for 48 hours. After washing with Sorensen's phosphate buffer, the stained bones were embedded in 1.5% agarose and placed in a 20-mm diameter tube and scanned using μCT40 scanner (Scanco Medical AG, Bassersdorf, Switzerland; 70 kVp, 114 μA, 300 ms integration time, 10 μm voxel size). Density measurements were calibrated to the manufacturer's hydroxyapatite phantom. Analysis was performed using the manufacturer's evaluation software and a threshold of 360 for MAT.

Histology and histomorphometry—Femur and Tibia were fixed in 10% neutral buffered formalin, followed by decalcification in 14% EDTA for 10 days, paraffin embedding, and TRAP staining. Histomorphometric parameters were measured using BioQuant OsteoII (BioQuant Image Analysis Corporation, Nashville, TN) in a blinded fashion.

Fat Transplantation—Mature fat depots were transplanted as described (Gavrilova et al., 2000) with slight modification. 2 month old DTR^{ADQ} or WT mice were anesthetized with isoflurane. Donor fat pads from 6–8 week old WT or DTR^{ADQ} mice were placed into sterile PBS and cut into 100–150mg pieces. The grafts were implanted subcutaneously through small incisions in the shaved skin of the back, with 1 piece per incisions. 6 pieces of fat graft were implanted into each FF mouse. After surgery the mice were housed individually for a week and then 5 mice per cage. Mice were sacrificed 2 months after transplantation.

Parabiosis—Female mice were housed together for 3 weeks before surgery which was performed by the mouse Cardiovascular Phenotyping Core at Washington University as previously described (Kamran et al., 2013). 2 months after surgery, paired mice were injected IP with DT daily for 10 days.

Ovariectomy—Female mice were 8-week old at time of OVX. Sham operated mice were anesthetized and similarly incised but ovaries were not removed. 20 days after surgery, mice were IP injected with or without Diphtheria Toxin daily for 10 days. Measurements were made 30 days after sham operation or OVX.

Biomechanics—Femora were scanned by μCT at the midshaft (Scanco μCT40; 70 kVp, 114 mA, 300 ms integration time, 10 um voxel size, 100 slices) to determine cross-sectional geometric properties. They were then mechanically tested to failure in three-point pending (Instron 8841; support span: 7 mm; displacement rate: 0.1 mm/sec). Failure occurred directly beneath the loading point, at the 50% length of the femur. Force-displacement data were collected and analyzed to determine whole-bone (structural) mechanical properties (stiffness, ultimate force, post-yield displacement, work-to-fracture).

RNA Sequencing and Analysis—Samples were prepared according to library kit manufacturer's protocol, indexed, pooled, and sequenced on an Illumina HiSeq. Basecalls and demultiplexing were performed with Illumina's bcl2fastq software and a custom python demultiplexing program with a maximum of one mismatch in the indexing read. RNA-seq

reads were then aligned to the Ensembl release 76 top-level assembly with STAR version 2.0.4b (Dobin et al., 2013). Gene counts were derived from the number of uniquely aligned unambiguous reads by Subread:featureCount version 1.4.5 (Liao et al., 2014). Sequencing performance was assessed for the total number of aligned reads, total number of uniquely aligned reads, and features detected. The ribosomal fraction, known junction saturation, and read distribution over known gene models were quantified with RSeQC version 2.3 (Wang et al., 2012).

All gene counts were then imported into the R/Bioconductor package EdgeR (Robinson et al., 2010) and TMM normalization size factors were calculated to adjust for samples for differences in library size. Ribosomal genes and genes not expressed in at least three samples greater than one count-per-million were excluded from further analysis. The TMM size factors and the matrix of counts were then imported into the R/Bioconductor package Limma (Ritchie et al., 2015). Weighted likelihoods based on the observed mean-variance relationship of every gene and sample were then calculated for all samples with the voomWithQualityWeights (Liu et al., 2015). The performance of all genes was assessed with plots of the residual standard deviation of every gene to their average log-count with a robustly fitted trend line of the residuals. Differential expression analysis was then performed to analyze for differences between conditions and the results were filtered for only those genes with Benjamini-Hochberg false-discovery rate adjusted p-values less than or equal to 0.05.

Significant genes with log 2 fold-changes greater than an absolute value of 2 and FDR <= 0.05 were separated into up and down regulated gene lists and subjected to CompBio analysis, which is accomplished with an automated Biological Knowledge Generation Engine (BKGE) that extracts all abstracts from PubMed that reference entities of interest (or their synonyms), using contextual language processing and a biological language dictionary that is not restricted to fixed pathway and ontology knowledge bases. Conditional probability analysis is utilized to compute the statistical enrichment of biological concepts (processes/pathways) over those that occur by random sampling. Related concepts built from the list of differentially expressed entities are further clustered into higher-level themes (e.g., biological pathways/processes, cell types and structures, etc.).

Within CompBio, scoring of gene, concept, and overall theme enrichment is accomplished using a multi-component function referred to as the Normalized Enrichment Score (NES) (Cowardin et al., 2019). The first component utilizes an empirical p-value derived from several thousand random entity lists of comparable size to the users input entity list to define the rarity of a given entity-concept event. The second component, effectively representing the fold enrichment, is based on the ratio of the concept enrichment score to the mean of that concept’s enrichment score across the set of randomized entity data. As such, the NES reflects both the rarity of the concept event associated with an entity list, as well as its degree of overall enrichment. Based on these empirical criteria, observed entity-concept scores above 10.0, 100.0, and 1,000.0 are labeled as moderate, marked, or high in level of enrichment above random. Themes scoring above 500.0, 1000.0, and 5000.0 are labeled similarly.

Immunofluorescence staining—Bones were further fixed with 10% neutral buffered formalin 24–48 hours at room temperature and partially decalcified in 14% EDTA for 3 days with daily change of solution. The bones were then infiltrated with 30% sucrose overnight at 4 °C for cryoprotection and embedded in optimal cutting temperature (Tissue-Tek). Sections of 10-μm thickness were prepared with a Leica cryostat equipped with Cryojane (Leica, IL). The sections were kept at −20 °C until use. The antibodies used in this study are as follows: phosphor-smad (13820, Cell Signal, 1:100), rabbit anti-TK (1:100), anti-PCNA (sc-56; Santa Cruz Biotechnology Inc.; 1:100). The secondary antibodies include goat anti-rabbit Alexa Fluor 594 (ThermoFisher Scientific, 1:200). Slides were mounted with antifade mounting medium with DAPI (Vector Laboratories), and images were acquired with a confocal microscope (Nikon C-1 confocal system).

Immunoblotting—After denaturing in sodium dodecyl sulfate (SDS), serum was subjected to 10% SDS–polyacrylamide gel electrophoresis and transferred to polyvinylidene difluoride transfer membranes. Cultured cells were washed twice with ice cold PBS and lysed in radioimmune precipitation assay (RIPA) buffer containing 20 mm Tris HCl, pH 7.5, 150 mm NaCl, 1 mm EDTA, 1 mm EGTA, 1% Triton X-100, 2.5 mm sodium pyrophosphate, 1 mm β-glycerophosphate, 1 mm Na3VO4, 1 mm NaF, and 1× protease inhibitor mixture (Roche Applied Science). After incubation on ice for 10 min, cell lysates were clarified by centrifugation at 15,000 rpm for 10 min. 40μg of total lysates were subjected to 8% sodium dodecyl sulfate polyacrylamide gel electrophoresis and transferred onto PVDF membranes. Filters were blocked in 0.1% casein in PBS for 1 h and incubated with primary antibodies at 4 °C overnight followed by probing with fluorescence labeled secondary antibodies (Jackson ImmunoResearch Laboratories). Proteins were detected with the Odyssey Infrared Imaging System (LI-COR Biosciences). Densitometry was analyzed with Image Studio Lite software (LI-COR Biosciences).

Bone stromal cells and In Vitro CFU-OB culture—The entire marrow cavity of the shafts (femora and tibiae) of 2-mo-old male mice was flushed by removing one of the epiphyses and centrifuging the bone at 1000 rpm for 15 s. The remaining bones were crashed by mechanical force and digested with 0.15% Collagenase P (Roche, Cat. 11249002001) for 30 mins at 37C. After hemolysis in a red blood cell lysis buffer (Gibco, Cat. A10492), the total cells was resuspended in αMEM and filtered through a 70-μm cell strainer. Cells were resuspended and 2×10^4 cells/well/ml were seeded in 12 well plate in α-MEM supplemented with 10% FCS, 50 μg/ml ascorbic acid, and 5 μM β-glycerophosphate. Cells were cultured for 5 days, then fixed in 4% formaldehyde, and stained for alkaline phosphatase using 1-Step NBT/BCIT kit (Thermo Scientific, Cat. 34042).

In vitro adipogenesis—The entire marrow cavity of the shafts (femora and tibiae) of 2-mo-old male mice was flushed by removing one of the epiphyses and centrifuging the bone at 1000 rpm for 15 s. After hemolysis in ACK lysing buffer (Gibco, Cat. A10492), the total cells was resuspended in αMEM containing 20% FCS and filtered through a 70-μm cell strainer. Cells were resuspended and cultured in tissue culture plate in α-MEM supplemented with 20% FCS for 2 weeks. Then cells were resuspended and seeded in α-

MEM supplemented with 10% FCS with or without adipocyte differentiation media (100nM Dexamethasone, 200μM indomethacin and 1μM insulin) for 8 days.

QUANTIFICATION and STATISTICAL ANALYSIS

Data Representation and Statistical Analysis—Data are expressed as mean ± SD. Statistical analyses were performed with Prism software version 8 (GraphPad Software) using unpaired Student's 2-tailed *t*-test, one-way or 2-way ANOVA test with Holm-Sidak post–hoc test with adjustment for multiple testing. In all experiments, statistical significance was considered when $P < 0.05$. * $P < 0.05$, ** $P < 0.01$, *** $P < 0.001$ in all experiments. Mice were assigned to different groups randomly. Experiments involving treatment with DT, chemicals or OPG were performed in a blinded fashion. All analysis including μCT, histomorphometry and serum ELISA were blinded. Exclusion criteria were based on animal well-being at the beginning of the study. No animals were excluded from the study. No power analysis was performed to determine the sample size. The sample size in each study was based on experience with our previous studies determining the bone phenotype in lipodystrophic mice (Zou et al., 2019).

Supplementary Material

Refer to Web version on PubMed Central for supplementary material.

Acknowledgements

This research was supported by the following grants from the National Institutes of Health, R01 AR047867 (M.J.S.), P30 AR074992 (M.J.S., S.L.T.), R37 AR046523 (S.L.T.), R01 DK111389 (S.L.T.). J.R.B. was supported by the NIH Office of the Director (DP5 OD028125), Burroughs Wellcome Fund (CAMS 1019648), and Children's Discovery Institute (MI-F-2019–795). We thank Heather Zannit, PhD, for providing 3.6Col1-tk breeders, and Michael Brodt of the WU Musculoskeletal Structure and Strength Core for supporting μCT and mechanical testing.

References

Ahn J, Serrano de la Pena L, Shore EM, and Kaplan FS (2003). Paresis of a bone morphogenetic protein-antagonist response in a genetic disorder of heterotopic skeletogenesis. J. Bone Joint Surg. Am 85-a, 667–674.

Al-Shawi R, Burke J, Jones CT, Simons JP, and Bishop JO (1988). A Mup promoter-thymidine kinase reporter gene shows relaxed tissue-specific expression and confers male sterility upon transgenic mice. Mol. Cell. Biol 8, 4821–4828. [PubMed: 2850469]

Appelman-Dijkstra NM, and Papapoulos SE (2016). From disease to treatment: from rare skeletal disorders to treatments for osteoporosis. Endocrine 52, 414–426. [PubMed: 26892377]

Black DM, Bilezikian JP, Ensrud KE, Greenspan SL, Palermo L, Hue T, Lang TF, McGowan JA, Rosen CJ, and Pa THSI (2005). One year of alendronate after one year of parathyroid hormone (1–84) for osteoporosis. N. Engl. J. Med 353, 555–565. [PubMed: 16093464]

Chandra A, Lan S, Zhu J, Siclari VA, and Qin L (2013). Epidermal growth factor receptor (EGFR) signaling promotes proliferation and survival in osteoprogenitors by increasing early growth response 2 (EGR2) expression. J. Biol. Chem 288, 20488–20498. [PubMed: 23720781]

Cosman F, Miller PD, Williams GC, Hattersley G, Hu MY, Valter I, Fitzpatrick LA, Riis BJ, Christiansen C, Bilezikian JP, et al. (2017). Eighteen Months of Treatment With Subcutaneous Abaloparatide Followed by 6 Months of Treatment With Alendronate in Postmenopausal Women With Osteoporosis: Results of the ACTIVExtend Trial. Mayo Clin. Proc 92, 200–210. [PubMed: 28160873]

Cowardin CA, Ahern PP, Kung VL, Hibberd MC, Cheng J, Guruge JL, Sundaresan V, Head RD, Barile D, Mills DA, et al. (2019). Mechanisms by which sialylated milk oligosaccharides impact bone biology in a gnotobiotic mouse model of infant undernutrition. Proc Natl Acad Sci U S A 116, 11988–11996. [PubMed: 31138692]

Ding L, and Morrison SJ (2013). Haematopoietic stem cells and early lymphoid progenitors occupy distinct bone marrow niches. Nature 495, 231–235. [PubMed: 23434755]

Dobin A, Davis CA, Schlesinger F, Drenkow J, Zaleski C, Jha S, Batut P, Chaisson M, and Gingeras TR (2013). STAR: ultrafast universal RNA-seq aligner. Bioinformatics 29, 15–21. [PubMed: 23104886]

Ducy P, Amling M, Takeda S, Priemel M, Schilling AF, Beil FT, Shen JH, Vinson C, Rueger JM, and Karsenty G (2000). Leptin inhibits bone formation through a hypothalamic relay: A central control of bone mass. Cell 100, 197–207. [PubMed: 10660043]

Elefteriou F, Takeda S, Ebihara K, Magre J, Patano N, Kim CA, Ogawa Y, Liu X, Ware SM, Craigen WJ, et al. (2004). Serum leptin level is a regulator of bone mass. Proc Natl Acad Sci U S A 101, 3258–3263. [PubMed: 14978271]

Esposito M, Mondal N, Greco TM, Wei Y, Spadazzi C, Lin SC, Zheng H, Cheung C, Magnani JL, Lin SH, et al. (2019). Bone vascular niche E-selectin induces mesenchymal-epithelial transition and Wnt activation in cancer cells to promote bone metastasis. Nat. Cell Biol 21, 627–639. [PubMed: 30988423]

Ferron M, Wei J, Yoshizawa T, Del Fattore A, DePinho RA, Teti A, Ducy P, and Karsenty G (2010). Insulin signaling in osteoblasts integrates bone remodeling and energy metabolism. Cell 142, 296–308. [PubMed: 20655470]

Gavrilova O, Marcus-Samuels B, Graham D, Kim JK, Shulman GI, Castle AL, Vinson C, Eckhaus M, and Reitman ML (2000). Surgical implantation of adipose tissue reverses diabetes in lipoatrophic mice. J. Clin. Invest 105, 271–278. [PubMed: 10675352]

Gazzerro E, Pereira RC, Jorgetti V, Olson S, Economides AN, and Canalis E (2005). Skeletal overexpression of gremlin impairs bone formation and causes osteopenia. Endocrinology 146, 655–665. [PubMed: 15539560]

Gazzerro E, Smerdel-Ramoya A, Zanotti S, Stadmeyer L, Durant D, Economides AN, and Canalis E (2007). Conditional deletion of gremlin causes a transient increase in bone formation and bone mass. J. Biol. Chem 282, 31549–31557. [PubMed: 17785465]

Hardy R, and Cooper MS (2009). Bone loss in inflammatory disorders. J. Endocrinol. 201, 309–320. [PubMed: 19443863]

Hesse E, Schroder S, Brandt D, Pamperin J, Saito H, and Taipaleenmaki H (2019). Sclerostin inhibition alleviates breast cancer-induced bone metastases and muscle weakness. JCI insight 5.

Higashiyama S, Iwamoto R, Goishi K, Raab G, Taniguchi N, Klagsbrun M, and Mekada E (1995). The membrane protein CD9/DRAP 27 potentiates the juxtacrine growth factor activity of the membrane-anchored heparin-binding EGF-like growth factor. J. Cell Biol 128, 929–938. [PubMed: 7876316]

Horne AM, Mihov B, and Reid IR (2018). Bone Loss After Romosozumab/Denosumab: Effects of Bisphosphonates. Calcif. Tissue Int 103, 55–61. [PubMed: 29445836]

Hu K, Sun H, Gui B, and Sui C (2017). Gremlin-1 suppression increases BMP-2-induced osteogenesis of human mesenchymal stem cells. Molecular medicine reports 15, 2186–2194. [PubMed: 28260028]

Jilka RL, O'Brien CA, Ali AA, Roberson PK, Weinstein RS, and Manolagas SC (2009). Intermittent PTH stimulates periosteal bone formation by actions on post-mitotic preosteoblasts. Bone 44, 275–286. [PubMed: 19010455]

Jolette J, Attalla B, Varela A, Long GG, Mellal N, Trimm S, Smith SY, Ominsky MS, and Hattersley G (2017). Comparing the incidence of bone tumors in rats chronically exposed to the selective PTH type 1 receptor agonist abaloparatide or PTH(1–34). Regul. Toxicol. Pharmacol 86, 356–365. [PubMed: 28389324]

Kajimura D, Lee HW, Riley KJ, Arteaga-Solis E, Ferron M, Zhou B, Clarke CJ, Hannun YA, DePinho RA, Guo XE, et al. (2013). Adiponectin regulates bone mass via opposite central and peripheral mechanisms through FoxO1. Cell Metab 17, 901–915. [PubMed: 23684624]

Kamran P, Sereti KI, Zhao P, Ali SR, Weissman IL, and Ardehali R (2013). Parabiosis in mice: a detailed protocol. Journal of visualized experiments : JoVE.

Krishnamurthy N, and Kurzrock R (2018). Targeting the Wnt/beta-catenin pathway in cancer: Update on effectors and inhibitors. Cancer Treat. Rev 62, 50–60. [PubMed: 29169144]

Laflamme C, Curt S, and Rouabhia M (2010). Epidermal growth factor and bone morphogenetic proteins upregulate osteoblast proliferation and osteoblastic markers and inhibit bone nodule formation. Arch. Oral Biol 55, 689–701. [PubMed: 20627196]

Lee JH, Jang SJ, Baek HR, Lee KM, Chang BS, and Lee CK (2015). Synergistic induction of early stage of bone formation by combination of recombinant human bone morphogenetic protein-2 and epidermal growth factor. Journal of tissue engineering and regenerative medicine 9, 447–459. [PubMed: 24764222]

Lee KY, Russell SJ, Ussar S, Boucher J, Vernochet C, Mori MA, Smyth G, Rourk M, Cederquist C, Rosen ED, et al. (2013). Lessons on conditional gene targeting in mouse adipose tissue. Diabetes 62, 864–874. [PubMed: 23321074]

Li Y, Zou W, Brestoff JR, Rohatgi N, Wu X, Atkinson JP, Harris CA, and Teitelbaum SL (2019). Fat-Produced Adipsin Regulates Inflammatory Arthritis. Cell reports 27, 2809–2816 e2803. [PubMed: 31167128]

Liao Y, Smyth GK, and Shi W (2014). featureCounts: an efficient general purpose program for assigning sequence reads to genomic features. Bioinformatics 30, 923–930. [PubMed: 24227677]

Lin GL, and Hankenson KD (2011). Integration of BMP, Wnt, and notch signaling pathways in osteoblast differentiation. J. Cell. Biochem 112, 3491–3501. [PubMed: 21793042]

Linder M, Hecking M, Glitzner E, Zwerina K, Holcmann M, Bakiri L, Ruocco MG, Tuckermann J, Schett G, Wagner EF, et al. (2018). EGFR controls bone development by negatively regulating mTOR-signaling during osteoblast differentiation. Cell Death Differ 25, 1094–1106. [PubMed: 29445126]

Liu R, Holik AZ, Su S, Jansz N, Chen K, Leong HS, Blewitt ME, Asselin-Labat ML, Smyth GK, and Ritchie ME (2015). Why weight? Modelling sample and observational level variability improves power in RNA-seq analyses. Nucleic Acids Res 43, e97. [PubMed: 25925576]

Lowery JW, and Rosen V (2018). The BMP Pathway and Its Inhibitors in the Skeleton. Physiol. Rev 98, 2431–2452. [PubMed: 30156494]

Ma J, Lu W, Chen D, Xu B, and Li Y (2017). Role of Wnt Co-Receptor LRP6 in Triple Negative Breast Cancer Cell Migration and Invasion. J. Cell. Biochem 118, 2968–2976. [PubMed: 28247948]

Marcellini S, Henriquez JP, and Bertin A (2012). Control of osteogenesis by the canonical Wnt and BMP pathways in vivo: cooperation and antagonism between the canonical Wnt and BMP pathways as cells differentiate from osteochondroprogenitors to osteoblasts and osteocytes. Bioessays 34, 953–962. [PubMed: 22930599]

McClung M (2013). Controversies in osteoporosis management: concerns about bisphosphonates and when are “drug holidays” required? Clin. Obstet. Gynecol 56, 743–748. [PubMed: 24177063]

McClung MR, Brown JP, Diez-Perez A, Resch H, Caminis J, Meisner P, Bolognese MA, Goemaere S, Bone HG, Zanchetta JR, et al. (2018). Effects of 24 Months of Treatment With Romosozumab Followed by 12 Months of Denosumab or Placebo in Postmenopausal Women With Low Bone Mineral Density: A Randomized, Double-Blind, Phase 2, Parallel Group Study. J. Bone Miner. Res 33, 1397–1406. [PubMed: 29694685]

Miyoshi E, Higashiyama S, Nakagawa T, Hayashi N, and Taniguchi N (1997). Membrane-anchored heparin-binding epidermal growth factor-like growth factor acts as a tumor survival factor in a hepatoma cell line. J. Biol. Chem 272, 14349–14355. [PubMed: 9162071]

Mukohira H, Hara T, Abe S, Tani-Ichi S, Sehara-Fujisawa A, Nagasawa T, Tobe K, and Ikuta K (2019). Mesenchymal stromal cells in bone marrow express adiponectin and are efficiently targeted by an adiponectin promoter-driven Cre transgene. Int. Immunol 31, 729–742. [PubMed: 31094421]

Nakamura K, Iwamoto R, and Mekada E (1995). Membrane-anchored heparin-binding EGF-like growth factor (HB-EGF) and diphtheria toxin receptor-associated protein (DRAP27)/CD9 form a

complex with integrin alpha 3 beta 1 at cell-cell contact sites. J. Cell Biol 129, 1691–1705. [PubMed: 7790364]

Ono M, Inkson CA, Kilts TM, and Young MF (2011). WISP-1/CCN4 regulates osteogenesis by enhancing BMP-2 activity. J. Bone Miner. Res 26, 193–208. [PubMed: 20684029]

Pereira RC, Economides AN, and Canalis E (2000). Bone morphogenetic proteins induce gremlin, a protein that limits their activity in osteoblasts. Endocrinology 141, 4558–4563. [PubMed: 11108268]

Rendina-Ruedy E, and Rosen CJ (2020). Lipids in the Bone Marrow: An Evolving Perspective. Cell Metab 31, 219–231. [PubMed: 31668874]

Ritchie ME, Phipson B, Wu D, Hu Y, Law CW, Shi W, and Smyth GK (2015). limma powers differential expression analyses for RNA-sequencing and microarray studies. Nucleic Acids Res 43, e47. [PubMed: 25605792]

Robinson MD, McCarthy DJ, and Smyth GK (2010). edgeR: a Bioconductor package for differential expression analysis of digital gene expression data. Bioinformatics 26, 139–140. [PubMed: 19910308]

Roeder E, Matthews BG, and Kalajzic I (2016). Visual reporters for study of the osteoblast lineage. Bone 92, 189–195. [PubMed: 27616604]

Rohatgi N, Zou W, Collins PL, Brestoff JR, Chen TH, Abu-Amer Y, and Teitelbaum SL (2018). ASXL1 impairs osteoclast formation by epigenetic regulation of NFATc1. Blood advances 2, 2467–2477. [PubMed: 30266822]

Roslan Z, Muhamad M, Selvaratnam L, and Ab-Rahim S (2019). The Roles of Low-Density Lipoprotein Receptor-Related Proteins 5, 6, and 8 in Cancer: A Review. Journal of oncology 2019, 4536302. [PubMed: 31031810]

Sassmann A, Offermanns S, and Wettschureck N (2010). Tamoxifen-inducible Cre-mediated recombination in adipocytes. Genesis (New York, N.Y. : 2000) 48, 618–625.

Schatoff EM, Leach BI, and Dow LE (2017). Wnt Signaling and Colorectal Cancer. Current colorectal cancer reports 13, 101–110. [PubMed: 28413363]

Scheller EL, Doucette CR, Learman BS, Cawthorn WP, Khandaker S, Schell B, Wu B, Ding SY, Bredella MA, Fazeli PK, et al. (2015). Region-specific variation in the properties of skeletal adipocytes reveals regulated and constitutive marrow adipose tissues. Nature communications 6, 7808.

Scheller EL, Troiano N, Vanhoutan JN, Bouxsein MA, Fretz JA, Xi Y, Nelson T, Katz G, Berry R, Church CD, et al. (2014). Use of osmium tetroxide staining with microcomputerized tomography to visualize and quantify bone marrow adipose tissue in vivo. Methods Enzymol 537, 123–139. [PubMed: 24480344]

Schneider MR, Sibilia M, and Erben RG (2009). The EGFR network in bone biology and pathology. Trends Endocrinol. Metab 20, 517–524. [PubMed: 19819718]

Shukla P, Mansoori MN, Kakaji M, Shukla M, Gupta SK, and Singh D (2017). Interleukin 27 (IL-27) Alleviates Bone Loss in Estrogen-deficient Conditions by Induction of Early Growth Response-2 Gene. J. Biol. Chem 292, 4686–4699. [PubMed: 28130449]

Takebe N, Miele L, Harris PJ, Jeong W, Bando H, Kahn M, Yang SX, and Ivy SP (2015). Targeting Notch, Hedgehog, and Wnt pathways in cancer stem cells: clinical update. Nature reviews. Clinical oncology 12, 445–464. [PubMed: 25850553]

Takemura T, Kondo S, Homma T, Sakai M, and Harris RC (1997). The membrane-bound form of heparin-binding epidermal growth factor-like growth factor promotes survival of cultured renal epithelial cells. J. Biol. Chem 272, 31036–31042. [PubMed: 9388253]

Troilo H, Barrett AL, Wohl AP, Jowitt TA, Collins RF, Bayley CP, Zuk AV, Sengle G, and Baldock C (2015). The role of chordin fragments generated by partial tolloid cleavage in regulating BMP activity. Biochem. Soc. Trans 43, 795–800. [PubMed: 26517884]

van Lierop AH, Appelman-Dijkstra NM, and Papapoulos SE (2017). Sclerostin deficiency in humans. Bone 96, 51–62. [PubMed: 27742500]

Voorneveld PW, Kodach LL, Jacobs RJ, van Noesel CJ, Peppelenbosch MP, Korkmaz KS, Molendijk I, Dekker E, Morreau H, van Pelt GW, et al. (2015). The BMP pathway either enhances or inhibits

the Wnt pathway depending on the SMAD4 and p53 status in CRC. Br. J. Cancer 112, 122–130. [PubMed: 25393365]

Wang C, Xiao F, Gan Y, Yuan W, Zhai Z, Jin T, Chen X, and Zhang X (2018). Improving Bone Regeneration Using Chordin siRNA Delivered by pH-Responsive and Non-Toxic Polyspermine Imidazole-4,5-Imine. Cell. Physiol. Biochem 46, 133–147. [PubMed: 29587276]

Wang L, Wang S, and Li W (2012). RSeQC: quality control of RNA-seq experiments. Bioinformatics 28, 2184–2185. [PubMed: 22743226]

Williams E, and Bullock AN (2018). Structural basis for the potent and selective binding of LDN-212854 to the BMP receptor kinase ALK2. Bone 109, 251–258. [PubMed: 28918311]

Xu W, Luo F, Wang Q, Tan Q, Huang J, Zhou S, Wang Z, Sun X, Kuang L, Jin M, et al. (2017). Inducible Activation of FGFR2 in Adult Mice Promotes Bone Formation After Bone Marrow Ablation. J. Bone Miner. Res 32, 2194–2206. [PubMed: 28650109]

Yamakawa S, and Hayashida K (2019). Advances in surgical applications of growth factors for wound healing. Burns & trauma 7, 10. [PubMed: 30993143]

Zhu J, Siclari VA, Liu F, Spatz JM, Chandra A, Divieti Pajevic P, and Qin L (2012). Amphiregulin-EGFR signaling mediates the migration of bone marrow mesenchymal progenitors toward PTH-stimulated osteoblasts and osteocytes. PLoS One 7, e50099. [PubMed: 23300521]

Zou W, Rohatgi N, Brestoff JR, Zhang Y, Scheller EL, Craft CS, Brodt MD, Migotsky N, Silva MJ, Harris CA, et al. (2019). Congenital lipodystrophy induces severe osteosclerosis. PLoS Genet 15, e1008244. [PubMed: 31233501]

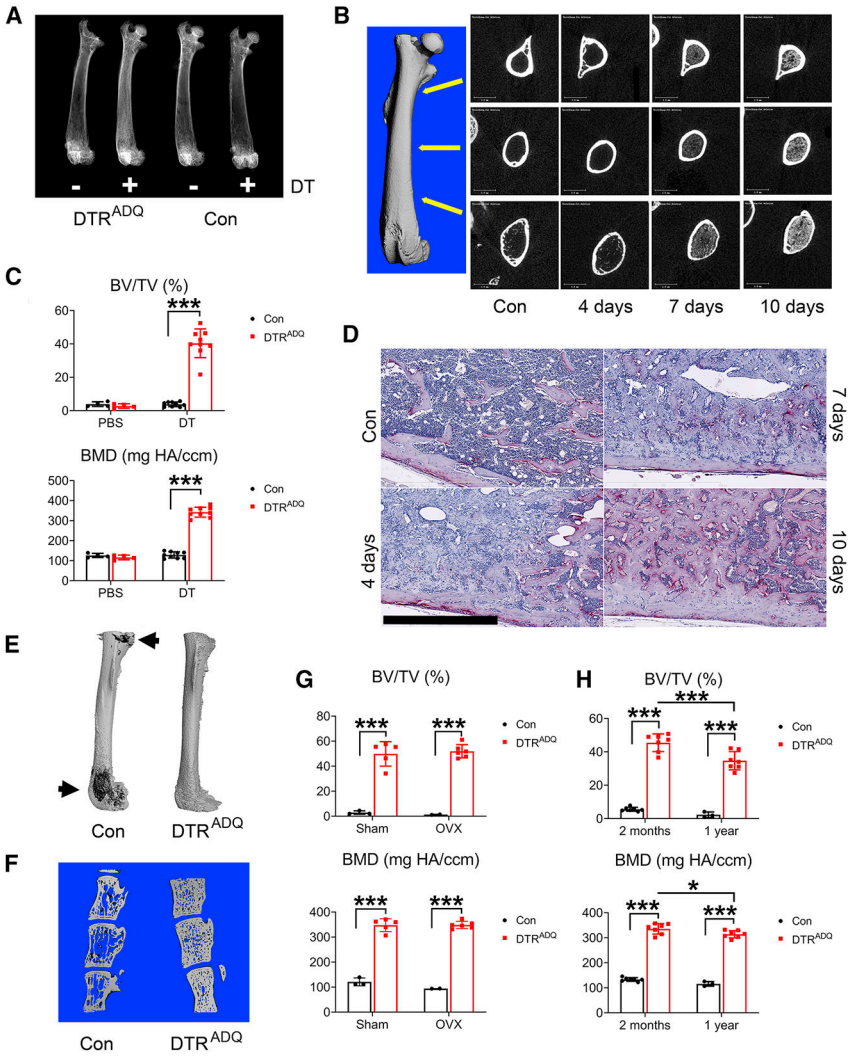

Fig 1. Adult fat ablated mice are osteosclerotic.

(A-F) 2 month old control (Con) or DTR^{ADQ} mice were daily injected with Diphtheria Toxin (DT) (100ng/mouse/day) or PBS.

(A) Representative radiographs of femurs after 10 days of DT or PBS injection. *n* = 6/group.

(B) Representative μCT images of DTR^{ADQ} femurs, extending from metaphysis to diaphysis, with time of DT injection. *n* = 6/group.

(C) Quantitative μCT analysis of whole femur of Con or DTR^{ADQ} mice after 10 days of DT or PBS injection. n = 4–9/group.

(D) Representative histological section of femur of 2 month old DTR^{ADQ} mice treated with DT with time. *n* = 5/group. Control (Con) received PBS for 10 days; Scale bar: 800 μm.

(E) Representative μCT images of osmium-stained femurs of Con and DTR^{ADQ} mice 4 days after DT injection. *n* = 5/group. Marrow fat in dark gray (arrows), decalcified bone overlaid in light grey.

(F) Representative μCT images of vertebrae (L3–5) of Con and DTR^{ADQ} mice 10 days after DT injection. *n* = 5/group.

(G) 2 month old Con or DTR^{ADQ} mice were subjected to ovariectomy or sham operation. 3 weeks after surgery, mice were daily injected with DT for 10 days. Whole femur BV/TV and BMD were analyzed by μCT. n = 2–6/group.
(H) 2 month or 1 year old Con or DTR^{ADQ} mice were daily injected with DT for 10 days. Whole femur was analyzed by μCT. n = 3–7/group.
Data are presented as mean ± SD. * $P < 0.05$, *** $P < 0.001$ as determined by 2 way ANOVA with Holm-Sidak's post hoc analysis for multiple comparisons test (C, G, H).

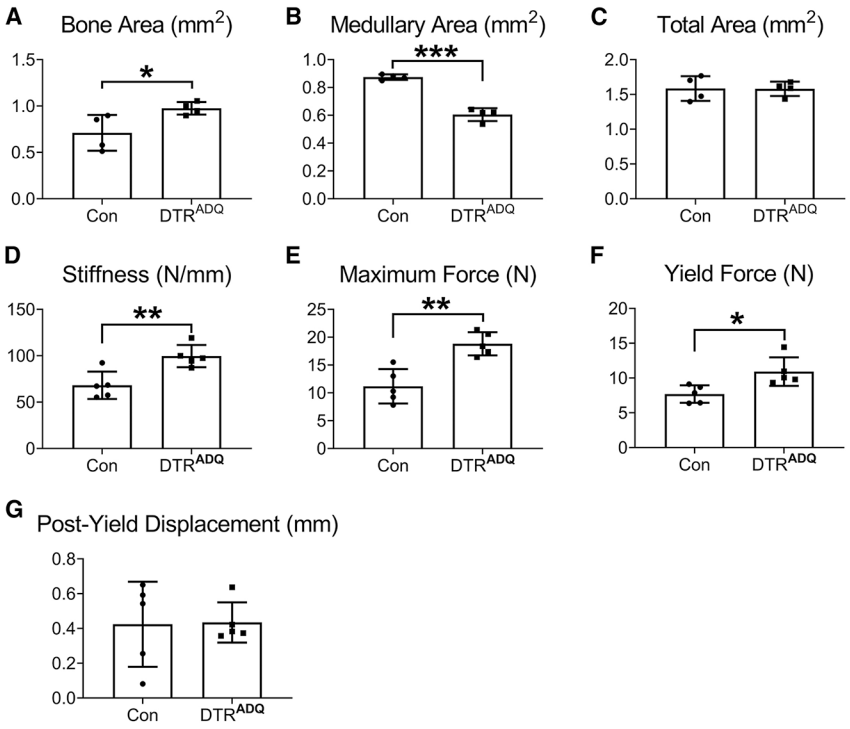

Fig 2. Post-natal fat ablation enhances bone strength.

2 month-old control (Con) or DTR^{ADQ} mice were daily injected with Diphtheria Toxin (DT) (100ng/mouse/day) for 10 days. μCT analysis of femoral (A) diaphyseal bone area, (B) medullary area and (C) total area. Bending tests analysis of femoral (D) stiffness, (E) maximum force (a measure of whole bone strength) and (F) yield force, (G) Post yield displacement. $n = 5$/group.

Data are presented as mean ± SD. * $P < 0.05$, ** $P < 0.01$, *** $P < 0.001$ as determined by unpaired t test.

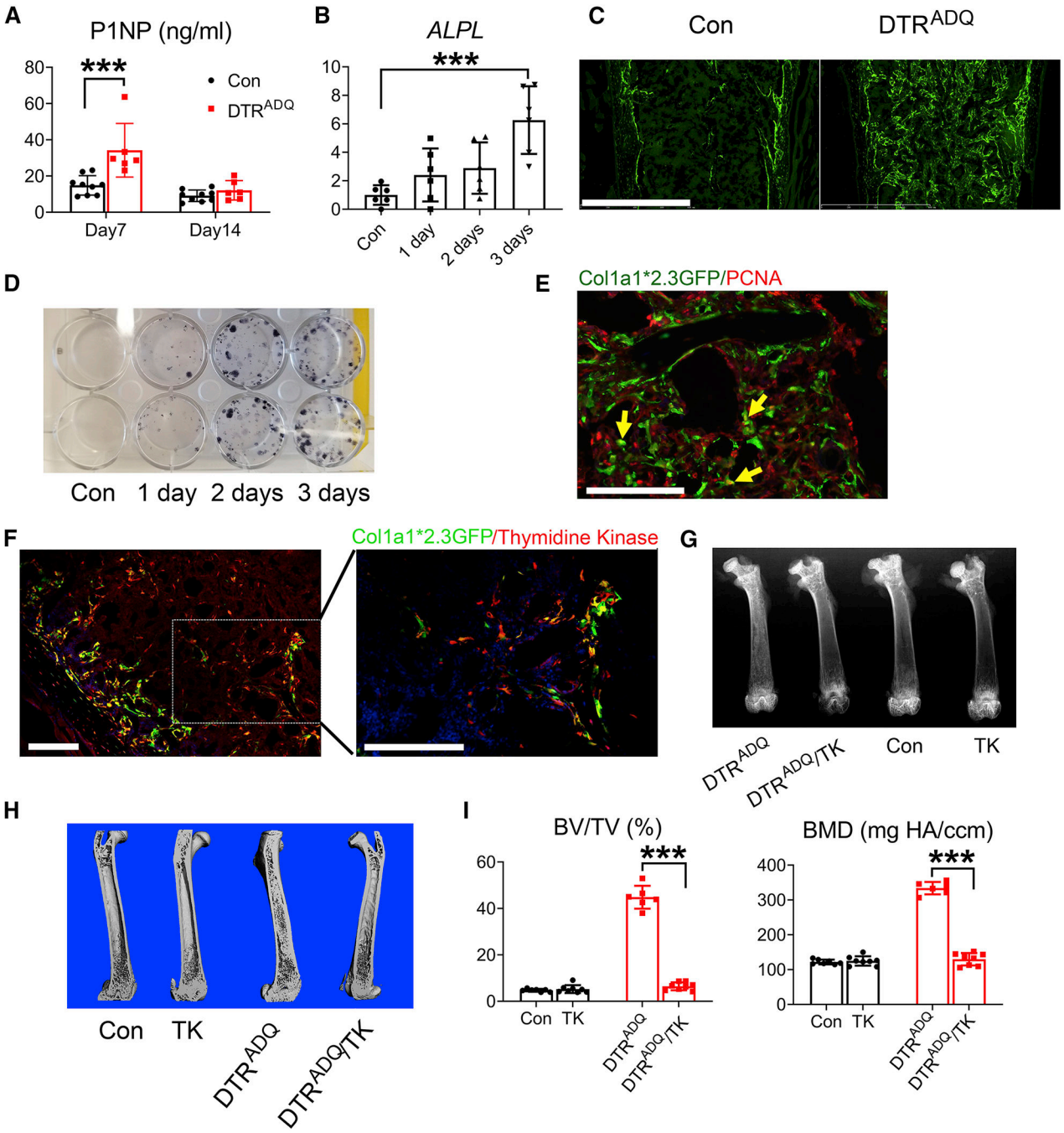

Fig 3. DT/DTR^{ADQ} osteosclerosis is due to enhanced osteoblast recruitment and differentiation.

(A) Serum P1NP of Con and DTR^{ADQ} mice after 7 days and 14 days of DT injection. n = 6–9/group.

(B) qPCR analysis of femoral marrow alkaline phosphatase mRNA of 2month old DTR^{ADQ} mice treated with DT with time. Con represents 3 days of PBS injection. n = 6/group.

(C) Representative fluorescent microscopic images of femoral diaphysis of DTR^{ADQ} mice mated to Col1a1*2.3GFP reporter mice treated with DT for 4 days. Con were mated to

Col1a1*2.3GFP reporter mice and treated with DT for 4 days. n = 4/group. Scale bar: 800 μm.

(D) CFU-OBs generated from crushed periosteum-stripped femur of DTR^{ADQ} mice treated with DT with time. No DT treatment serves as Con. n = 3 independent experiments.

(E) PCNA (red) fluorescent immunohistochemical staining of femoral diaphysis of DTR^{ADQ}/Col1a1*2.3 GFP mice treated with DT for 4 days. Arrows indicate occasional cells (yellow) expressing both PCNA and GFP. n = 4/group. Scale bar: 100 μm

(F) Thymidine Kinase (TK) fluorescent immunohistochemical staining (red) of femoral diaphysis of DTR^{ADQ}/Col1a1*2.3 GFP/Col1a1*3.6-TK mice treated with DT for 4 days. n = 4/group. Scale bar: 100 μm.

(G-I) Con or DTR^{ADQ} mice were mated with Col1a1*3.6 -TK mice. At 2 months of age all genotypes were treated with DT and Ganciclovir for 10 days. G) Representative radiographs of femurs; H) Representative μCT images of femurs; I) Quantitative μCT analysis of whole femur of H. n = 6–8/group.

Data are presented as mean ± SD. * $P < 0.05$, *** $P < 0.001$ as determined by 1 way (B) or 2 way (A, I) ANOVA with Holm-Sidak's post hoc analysis for multiple comparisons test.

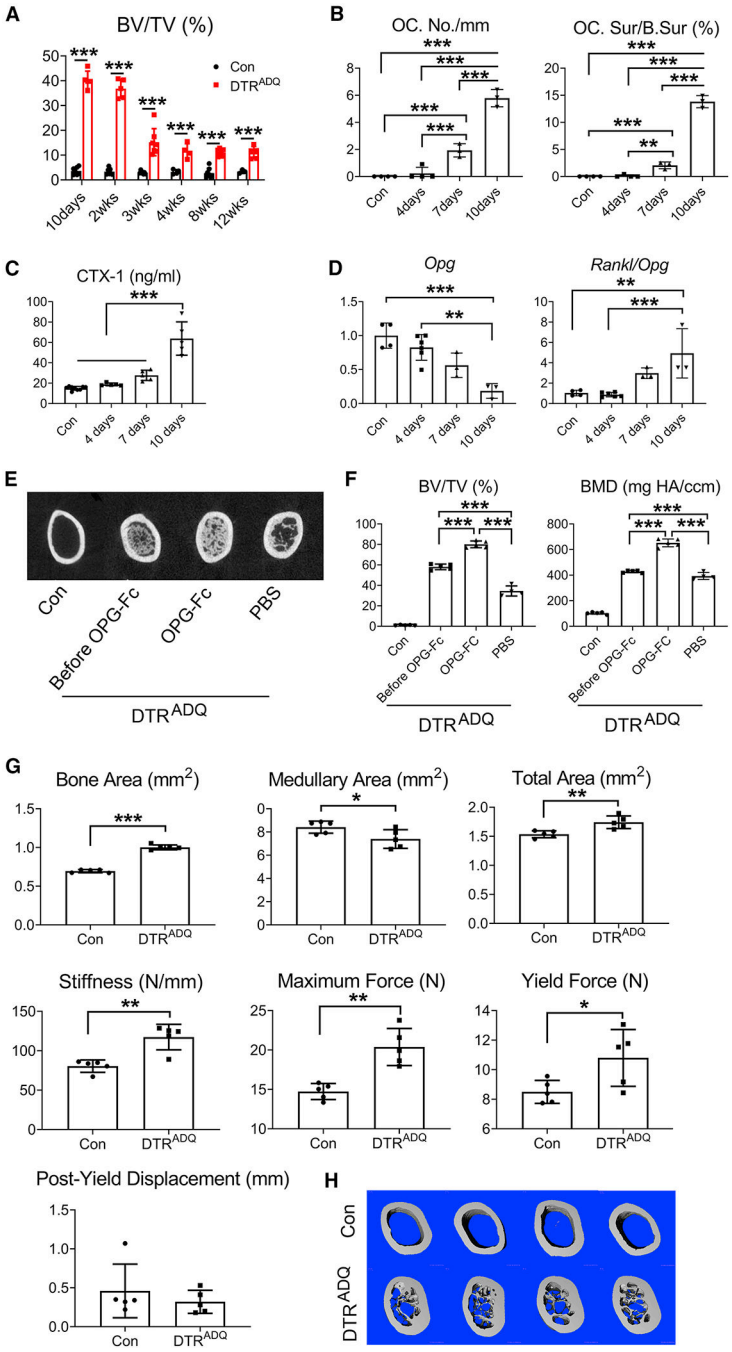

Fig 4. Anti-resorptive therapy maintains DT/DTR^{ADQ}-mediated osteosclerosis.

(A) Quantitative μCT analysis of whole femur of Con and DTR^{ADQ} mice treated with DT daily with time. n = 3–8/group.

(B) Histomorphometric analysis of osteoclast number/mm bone surface and osteoclast surface/bone surface in femoral diaphysis of DTR^{ADQ} mice treated with DT with time. No DT treatment serves as control. n = 3–4/group.

(C) Serum CTX-1 of DTR^{ADQ} mice treated with DT daily with time. Non DT injected DTR^{ADQ} mice serve as control. n = 5–9/group.

(D) qPCR analysis of femoral bone OPG mRNA and Rankl/OPG ratio of 2month old DTR^{ADQ} mice treated with DT with time. No DT treatment DTR^{ADQ} mice serve as control. $n = 3–6$/group.

(E-F) 2 months old Con or DTR^{ADQ} mice treated with DT for 10 days (Before OPG-Fc) or DTR^{ADQ} mice treated with DT, with or without OPG-Fc, for an additional 20 days. (E) Representative μCT image of femoral diaphysis; F) Whole femur quantitative μCT analysis. $n = 4–5$/group.

(G-H) Control (Con) or DTR^{ADQ} mice were daily injected with Diphtheria Toxin (DT) (100ng/mouse/day) for 2 months. (G) μCT analysis of femoral diaphyseal bone area, medullary area and total area. Bending tests analysis of femoral stiffness, maximum force, yield force and post yield displacement. $n = 5$/group. (H) Representative μCT image of femoral diaphysis of Con or DTR^{ADQ} mice treated with DT for 2 months. $n = 5$/group. Data are presented as mean ± SD. * $P < 0.05$, ** $P < 0.01$, *** $P < 0.001$ as determined by unpaired t test (G), 1 way (B,C,D, F) or 2 way (A) ANOVA with Holm-Sidak's post hoc analysis for multiple comparisons test.

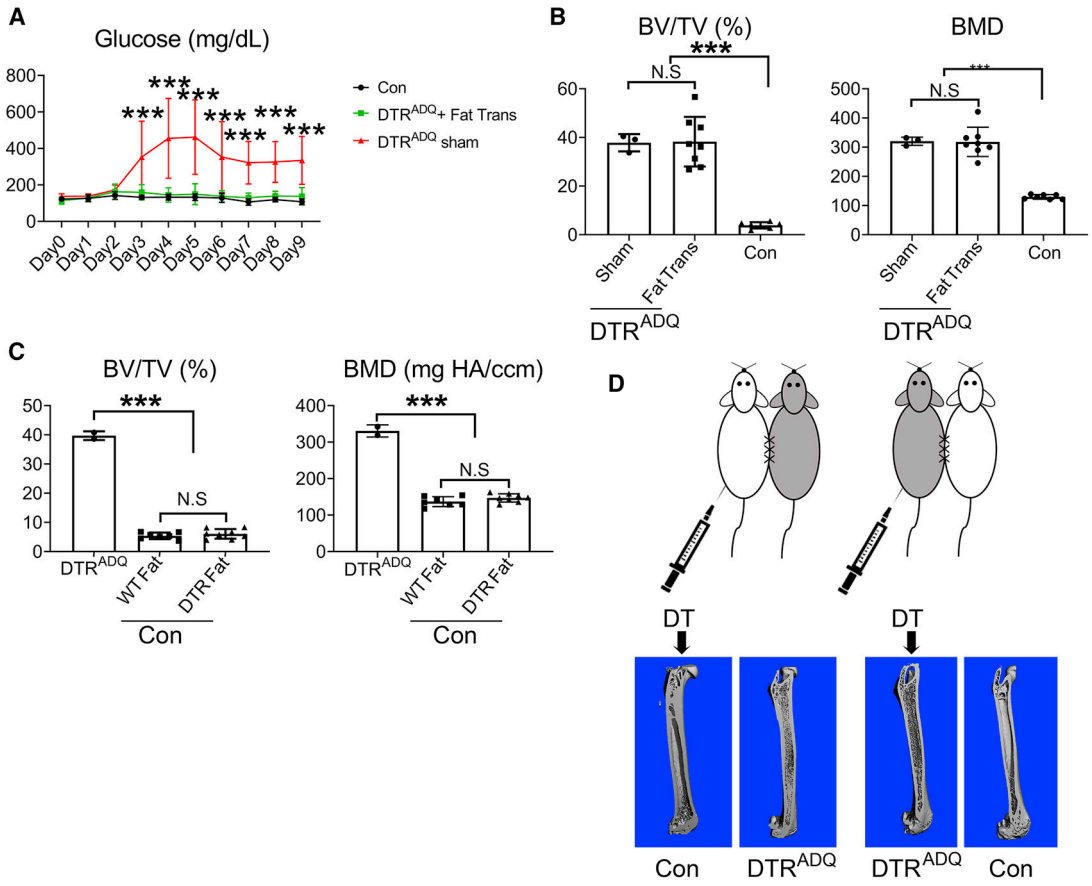

Fig 5. DT/DTR^{ADQ}-induced osteogenesis is not mediated by loss of peripheral adipose tissue.

(A) 2 months after WT WAT transplantation, mice were administrated DT daily. WT (Con) and sham operated DTR^{ADQ} mice serve as controls. Serum glucose was measured before (Day0) or after DT daily treatment (Day1- Day9). n = 4–8/group.

(B) Quantitative μCT analysis of whole femur of DTR^{ADQ} mice 2 months after WT WAT transplantation, treated with DT for 10 days. WT (Con) and sham operated DTR^{ADQ} mice serve as controls. n = 3–8/group.

C) Quantitative μCT analysis of whole femur of WT mice 2 months after WT or DTR^{ADQ} WAT transplantation treated with DT for 10 days. Non-transplanted DTR^{ADQ} mice serve as control. n = 2–8/group.

(D) 2 month old control and DTR^{ADQ} female mice were parabiosed. 2 months after surgery, DT was directly injected into Con or DTR^{ADQ} mice as indicated for 10days. n = 3 pairs/group. Upper panel: the scheme of parabiosis experiment; Lower panel: representative μCT images of femurs of Con and DTR^{ADQ} mice of each partner.

Data are presented as mean ± SD. * $P < 0.05$, *** $P < 0.001$ as determined by 1 way (B, C) or 2 way (A) ANOVA with Holm-Sidak's post hoc analysis for multiple comparisons test.

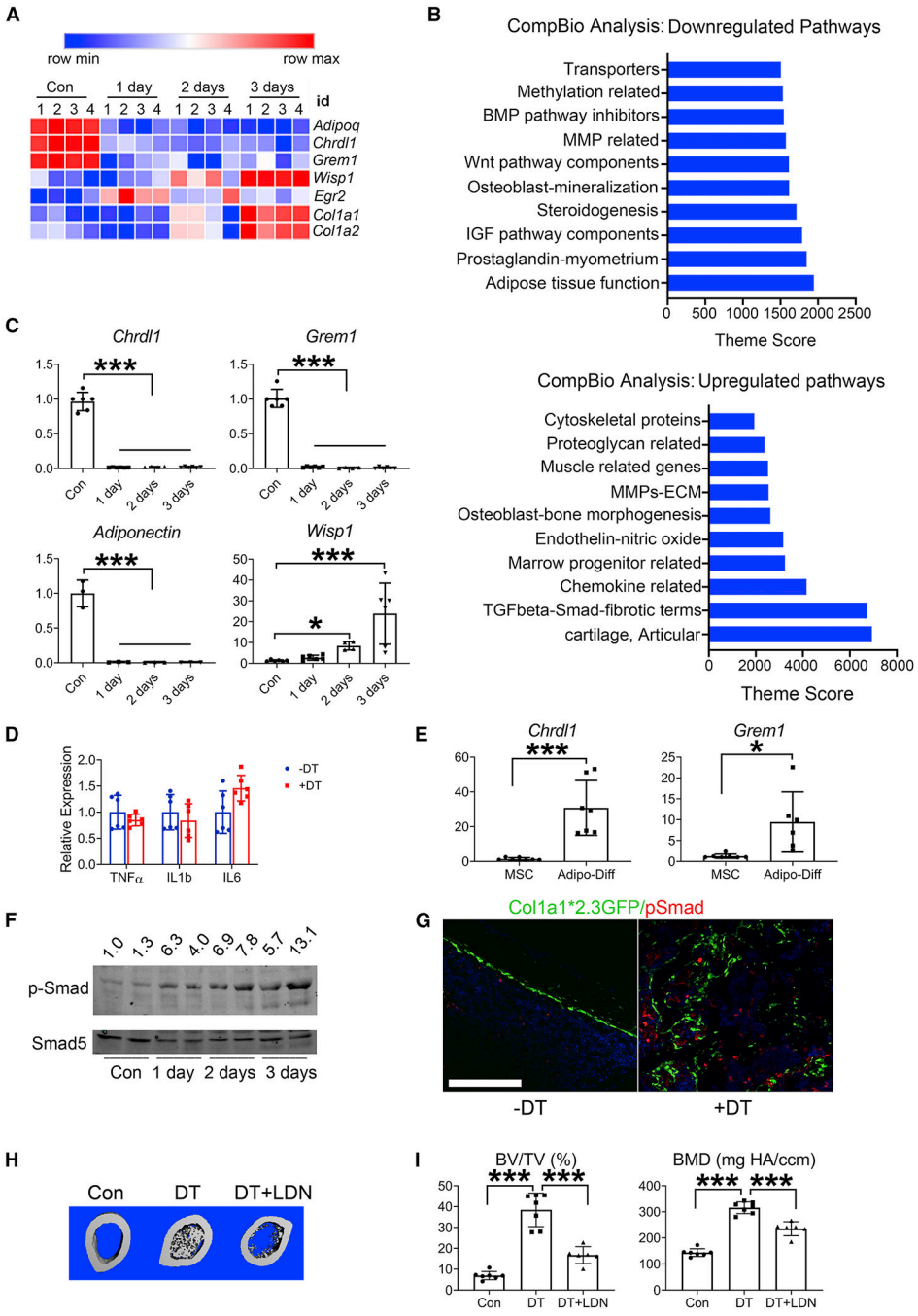

Fig 6. BMPR signaling mediates adipocyte ablation-induced osteogenesis.

(A) Heatmap of RNA sequencing of bone marrow mRNAs of DTR^{ADQ} mice treated with or without (Con) DT with time.

(B) CompBio analysis of downregulated and upregulated pathways of RNA sequencing of bone marrow mRNA of DTR^{ADQ} mice treated with or without DT for 3 days.

(C) qPCR analysis of *Chrdl1, Grem1, Adiponectin* and *Wisp1* mRNA in femoral bone marrow of 2 month old DTR^{ADQ} mice treated with DT with time; Con received no DT. n = 3–6/group.

(D) qPCR analysis of inflammatory cytokine mRNA in femoral bone marrow of 2 month old DTR^{ADQ} mice treated with or without DT for 3 days. $n = 6$/group.
(E) Marrow stromal cells were cultured in the presence (Adipo-Diff) or absence (MSC) of adipocyte differentiation media for 8 days. *Chrdl1* and *Grem1* gene expression was analyzed by qPCR. $n = 6–7$/group.
(F) immuno-blot analysis of Phospho-$Smad_{1,5,8}$ in whole bone marrow lysates of DTR^{ADQ} mice treated with DT with time. Con received no DT. Densitometric analysis is performed relative to Smad 5. $n = 3$ independent experiments.
(G) Representative fluorescent microscopic images of phosphor-$Smad_{1,5,8}$ (red) immunohistochemical staining of distal femur of DTR^{ADQ}/Col1a1*2.3 GFP mice treated with or without DT for 4 days. $n = 3$/group. Scale bar: 100 μm.
(H) Representative μCT images of femoral diaphysis of DTR^{ADQ} mice treated with DT with or without LDN193189 for 10 days. No DT treatment serves as control. $n = 6–7$/group.
(I) Whole femur quantitative μCT analysis of (G). $n = 6–7$/group.
Data are presented as mean ± SD. * $P < 0.05$, *** $P < 0.001$ as determined by unpaired t test (D, E) or 1 way ANOVA with Holm-Sidak's post hoc analysis for multiple comparisons test (C, I).

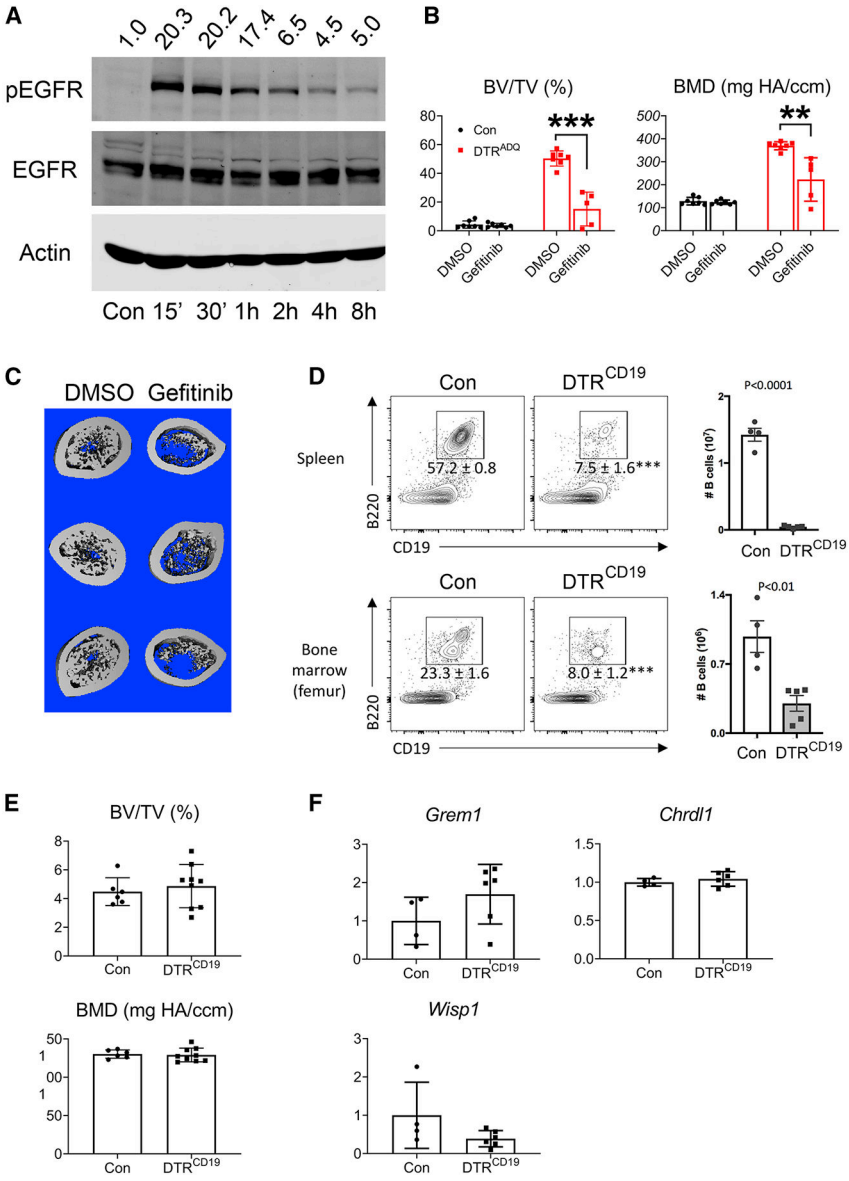

Fig 7. EGFR and BMPR signaling partner to promote osteogenesis.

(A) ST2 cells were treated with HB-EGF (5ng/ml) for indicated time and pEGFR was detected by immunoblot. Actin and EGFR serve as loading controls. Densitometric analysis is performed relative to EGFR. *n* = 3 independent experiments.

(B) Quantitative μCT analysis of whole femur of DTR^{ADQ} mice treated with DT in the presence or absence of Gefitinib (100mg/Kg) daily for 10 days. *n* = 5–7/group.

(C) μCT images of femoral diaphysis of (B). *n* = 5–7/group.

(D) Con and DTR^{CD19} mice were treated with DT daily for 3 days. Upper panel: Left: FACS plots of CD19+ B220+ B cells in the spleen, pre-gated on CD45+ cells. Numbers show frequencies of CD45+ cells that are B cells. Right: Numbers of CD45+ CD19+ B220+ B cells in the spleen. Lower panel: Left: FACS plots of CD19+ B220+ B cells in the femur bone marrow, pre-gated on CD45+ cells. Numbers show frequencies of CD45+ cells that are

B cells. Right: Numbers of CD45+ CD19+ B220+ B cells in the bone marrow. n = 4–5/group.

(E) Quantitative μCT analysis of whole femur of Con and DTR^{CD19} mice after treated with DT daily for 10 days. n = 6–9/group.

(F) Con and DTR^{CD19} mice were treated with DT daily for 3 days. qPCR analysis of femoral marrow Chrdl1, Grem1 and Wisp1 mRNA. n = 4–6/group.

Data are presented as mean ± SD. ** $P < 0.01$, *** $P < 0.001$ as determined by unpaired t test (D-F) or 1 way ANOVA with Holm-Sidak's post hoc analysis for multiple comparisons test (B).

Key Resources Table

REAGENT or RESOURCE	SOURCE	IDENTIFIER
Antibodies		
Rabbit anti-phospho-smad	Cell Signaling Biotechnology	Cat# 13820; RRID: AB_2493181
Rabbit anti-Smad5	Cell Signaling Biotechnology	Cat# 12534; RRID: AB_2797946
Rabbit anti-Adiponectin	Cell Signaling Biotechnology	Cat# 2789; RRID: AB_2221630
Rabbit anti-phospho EGFR	Cell Signaling Biotechnology	Cat# 3777; RRID: AB_2096270
Rabbit anti-EGFR	Cell Signaling Biotechnology	Cat# 2232; RRID: AB_331707
Mouse anti-PCNA	Santa Cruz Biotechnology	Cat# SC-56; RRID: AB_628110
Mouse anti-Actin	Sigma Aldrich	Cat# A2228; RRID: AB_ 476697
Rabbit anti-Thymidine kinase	William Summers (Yale)	N/A
Rat anti-mouse B220-PE	BioLegend	Clone RA3-6B2; RRID: AB_312993
Rat anti-mouse CD45-APC	BioLegend	Clone 30-F11 ; RRID: AB_312976
Rat anti-mouse CD19 APC/Fire750	BioLegend	Clone 6D5; RRID: AB_2572120
FcBlock	BD Biosciences	Clone 24G.2; RRID: AB_394656
Chemicals, Recombinant Proteins		
Diphtheria Toxin	Biological List Laboratories	Cat #150
Tamoxifen	Sigma Aldrich	Cat# T5648
LDN193189	Sigma Aldrich	Cat# SML0559
XAV939	Selleckchem	Cat# S1180
Gefitinib	ApeBio	Cat# A8219
Ganciclovir	Acros Organics	Cat# 461710050
TRIzol Reagent	ThermoFisher Scientific	Cat# 15596026
Osmium Tetroxide 4% solution	Electron Microscopy Sciences	Cat# 19170
Sorensen’s Phosphate buffer	Electron Microscopy Sciences	Cat# 11600-10
Collagenase P	Roche	Cat# 11249002001
Ascorbic Acid	Sigma Aldrich	Cat# A5960
β-glycerophosphate	Sigma Aldrich	Cat# G9422
Indomethacin	Sigma Aldrich	Cat# I7378
Dexamethasone	Sigma Aldrich	Cat# D4902
Insulin	Sigma Aldrich	Cat# I2643
OPG-Fc	Amgen Biotechnology	N/A
Recombinant Human HB-EGF	R&D Systems	Cat# 259-HE-050
MEM Alpha	Gibco	Cat# 12561-049
FBS	Gibco	Cat# 26140
0.05% Trypsin-EDTA	Gibco	Cat# 25300-054
Pen Strep	Gibco	Cat# 15140-122
30% Acrylamide/Bis Solution	Bio-Rad	Cat# 161-0158
Halt^{tm} Protease & Phosphatase inhibitor	Thermo Scientific	Cat# 78443

REAGENT or RESOURCE	SOURCE	IDENTIFIER
50% Dextrose	Hospira	Cat# 0409-6648-02
Oligonucleotides		
See Supplemental Table 3, 4		
Critical Commercial Assays		
iScript™ cDNA synthesis kit	Bio-Rad	Cat# 170-8891
Powerup™ SYBR™ Green	Applied Biosystems	Cat# 25742
Serum CTX-1 (RatLaps) RIA kit	Immunodiagnosticsystems	Cat# AC—06F1
Mouse P1NP EIA kit	Immunodiagnosticsystems	Cat# AC-33F1
RNeasy Mini kit	Qiagen	Cat# 74104
LDH activity Assay kit	BioVision Incorporated	Cat# K726-500
Deposited Data		
RNA sequencing data	GEO	GEO: GSE154800
Experimental Models: Organisms/Strains		
iDTR (Lox-Stop-Lox-ROSA-DTR)	The Jackson Laboratory	Stock No: 007900
Col1a1*2.3GFP	The Jackson Laboratory	Stock No: 013134
CD19 Cre	The Jackson Laboratory	Stock No: 006785
Adipoq Cre	The Jackson Laboratory	Stock No: 010803
Adipoq Cre/ERT2	The Jackson Laboratory	Stock No: 025124
TK-3.6Col1a1	Robert Jilka and Charles O'Brien (University of Arkansas) (Jilka et al., 2009)	N/A
Rosa-DTA (Lox-Stop-Lox-ROSA-DTA)	The Jackson Laboratory	Stock No: 010527
Experimental Models: Cell Line		
ST2	ATCC	CVCL-2205
Software and Algorithms		
GraphPad Prism 8	GraphPad	RRID:SCR_002798
Bioquant Osteo V7 10.10	Bioquant	RRID:SCR_016423
Image Studio Lite Ver4.0	LI-COR Biosciences	RRID:SCR_013715
STAR v2.0.4b	STAR	RRID:SCR_015899
Subread v1.4.5	Subread	RRID:SCR_009803
R v3.4.1	R	RRID:SCR_001905
EdgeR v3.20.2	Edger	RRID:SCR_012802
LIMMA v3.34.4	LIMMA	RRID:SCR_010943
RSeQC v2.3	RSeQC	RRID:SCR_005275
CompBio	http://www.percayai.com	N/A
Other		
Immobilon-FL PVDF transfer membranes	Millipore	Cat# IPFL00010
Contour Blood Glucose Strips	ASCENSIA Diabetes Care	Cat# 7097C
Contour Blood Glucose Meter	Bayer Health LLC	Cat# 9556C
BD Serum Separator Tubes	Becton, Dickinson and Company	Cat# 365967
Plain Capillary Tubes	Kimble Chase Life Science	Cat# 2502